Micaela dos Santos Cunha

RADIOBIOLOGY WITH PROTON CYCLOTRON BEAMS: A VIABILITY STUDY

Dissertação de Mestrado na área científica de Engenharia Biomédica, especialidade Imagem e Radiação, orientada pelo Professor Doutor Rui Ferreira Marques, Professor Doutor Francisco Alves e Professor Doutor Paulo Crespo e apresentada ao Departamento de Física da Faculdade de Ciências e Tecnologia da Universidade de Coimbra.

Setembro de 2010

UNIVERSIDADE DE COIMBRA

Radiobiology With Proton Cyclotron Beams: A Viability Study

Faculty of Sciences and Technology
University of Coimbra

To obtain the degree
of Master of Science in Biomedical Engineering

M.Sc. dissertation Micaela dos Santos Cunha
from Santo Tirso, Portugal

Coimbra 2010

Supervisor:	Prof. Dr. Rui Ferreira Marques
Co-supervisor:	Prof. Dr. Paulo Crespo
Co-supervisor:	Prof. Dr. Francisco Alves

Submission date:	06.09.2010
Public examination date:	14.09.2010

Para os que sempre me apoiaram.

Index

List of Figures

List of Tables

List of Acronyms and Abbreviations

2D / 3D	2 Dimension(al) / 3 Dimension(al)
ASR	Age-Standardized Rate
CATANA	Centro di AdroTerapia e Applicazioni Nucleari Avanzate, Catania, Italy
DNA	Deoxyribonucleic Acid
EBRT	External Beam Radiation Therapy
FTPI	Florida Proton Therapy Institute, Jacksonville, FL, USA
FWHM	Full Width at Half Maximum
GSI	Gesellschaft für Schwerionenforschung, Darmstadt, Germany
HIBMC	Hyogo Ion Beam Medical Center, Hyogo, Japan
HIT	Heavy Ion Therapy, Heidelberg, Germany
HMI	Hahn-Meitner-Institut Berlin, Berlin, Germany
HZB	Helmholtz Zentrum Berlin für Materialien und Energie, Berlin, Germany
IBA	Ion Beam Applications, S.A., Louvain-la-Neuve, Belgium
ICNAS	Instituto de Ciências Nucleares Aplicadas à Saúde, Coimbra, Portugal
IMRT	Intensity Modulated Radiation Therapy
IMPT	Intensity Modulated Proton Therapy
INFN-LNS	Istituto Nazionale di Fisica Nucleare - Laboratori Nazionali del Sud, Catania, Italy
ITEP	Institute for Theoretical and Experimental Physics, Moscow, Russia
LBNL	Lawrence Berkeley National Laboratory, Berkeley, CA, USA
LET	Linear Energy Transfer
LINAC	Linear Accelerator
LIP	Laboratório de Instrumentação e Física Experimental de Partículas, Coimbra, Portugal
MCS	Multiple Coulomb Scattering
MGH	Massachusetts General Hospital, Boston, MA, USA
MPRI	Midwest Proton Radiotherapy Institute, Bloomington, IN, USA
NCC	National Cancer Center, Kashiwa, Japan
NCC	National Cancer Center, Ilsan, South Korea
NPTC	Northeast Proton Treatment Center, Boston, MA, USA

OAR	Organ at Risk
PET	Positron Emission Tomography
PMRC	Proton Medical Research Center, Tsukuba, Japan
PTV	Planning Treatment Volume
PSI	Paul Scherrer Institute, Villigen, Switzerland
RBE	Relative Biological Effectiveness
RPC	Resistive Plate Chamber
RPTC	Rinecker Proton Therapy Center, Munich, Germany
SOBP	Spread-Out Bragg Peak
SRIM	The Stopping and Range of Ions in Matter
TRIM	The Transport of Ions in Matter
TRIUMF	TRI-University Meson Facility, Vancouver, Canada
UCSF	University of California, San Francisco, CA, USA
WERC	The Wakasa Wan Energy Research Center, Tsuruga, Japan
WPTC	Wanjie Proton Therapy Center, Zibo, China

Sumário

Motivação

O número de centros de radioterapia com protões está a aumentar em todo o mundo, com trinta centros actualmente em operação e mais de vinte em fase de planeamento ou já em construção. Os resultados da radioterapia com protões estão a despertar o interesse de cada vez mais centros médicos, num número crescente de países, em disponibilizá-la aos seus doentes. Ao mesmo tempo, ciclotrões capazes de acelerar protões até cerca de 20 MeV têm sido instalados por todo o mundo. Embora o seu propósito seja principalmente a produção de radioisótopos para tomografia por emissão de positrões, eles estão equipados com várias linhas de feixe que podem ser utilizadas para investigação científica. Cada linha de feixe pode dar tipicamente correntes de 150 μA (1x10^{15} partículas/s). Fazer estudos radiobiológicos usando estas linhas de feixe pode contribuir para o melhoramento dos resultados da radioterapia com protões, nomeadamente por dar novos dados para a resposta a algumas questões ainda por esclarecer:

- o impacto do fraccionamento da radioterapia com partículas na eficácia da dose, incluindo os diferentes efeitos nas regiões irradiadas no pico de Bragg versus no patamar;
- a influência das respostas dos tecidos vivos, como o edema, o encolhimento do tumor, o dano vascular com consequente permeabilidade aumentada, e processos inflamatórios com consequentes alterações na densidade dos tecidos;
- o efeito adjuvante e/ou tóxico do uso de compostos farmacêuticos em concomitância com a radioterapia;
- as causas da hipersensibilidade a baixas doses de radiação [Ste07b, Sch10];
- os mecanismos por detrás do efeito bystander ou efeito bystander induzido por radiação, e das chamadas respostas adaptativas [Mot04, Wid09]; e
- a evolução espacial e temporal do dano provocado pela radiação, a qual pode ser avaliada através da evolução espacial e temporal das quebras da cadeia dupla de ADN [Sch10].

Novos dados para responder a estas e outras questões podem contribuir para a melhoria dos resultados da radioterapia e consequentemente para a redução das taxas de mortalidade em doentes com cancro.

Neste trabalho estudamos a viabilidade da implementação de um sistema experimental numa das linhas de feixe do ciclotrão de 18 MeV recentemente instalado no Instituto de Ciências Nucleares Aplicadas à Saúde, Universidade de Coimbra. Esse sistema deve permitir a realização de estudos radiobiológicos, incluindo os efeitos da irradiação com protões em culturas celulares e animais de pequeno porte.

Várias simulações baseadas em Monte Carlo foram desenvolvidas no Geant4 para optimizar o sistema em estudo. Estas foram inicialmente validadas contra outro software como o SRIM/TRIM

e também contra resultados teóricos publicados. Os cálculos de dose foram feitos usando diferentes configurações para avaliar perfis de dose-profundidade e distribuições 2D.

Summary

Motivation

The number of proton radiotherapy facilities is increasing througout the world, with thirty centers currently operational and more than twenty in a planning stage or already under construction. Proton therapy outcomes are triggering the interest of more and more medical facilities, of a crescent number of countries, in making it available for their patients. At the same time, cyclotrons capable of accelerating protons up to about 20 MeV have been worldwide installed. Although their purpose is mainly positron emission tomography radioisotope production, they are equipped with several beam lines that may be used for scientific research. Each beam line may typically deliver proton currents up to 150 μA (1x10^{15} particles/s). Radiobiological studies using of these beam lines may contribute to further improve proton therapy results, namely by giving input to some unclear questions, namely:

- the impact of fractionation of particle radiotherapy on dose effectiveness including different effects in regions irradiated in the Bragg peak versus the plateau;
- the influence of living tissue responses such as edema, tumor shrinkage, vascular damage with consequent increased permeability, and inflammatory processes with consequent changes in tissue density;
- the adjuvant and/or toxic effects of using pharmaceutical compounds in concomitance with radiotherapy;
- the causes of hypersensitivity to low doses of radiation, a phenomenon called low-dose hyper-radiosensitivity [Ste07b, Sch10];
- the mechanisms underlying the bystander effect or radiation-induced bystander effect and the so-called adaptative responses [Mot04, Wid09]; and
- the spatial and temporal evolution of radiation damage, which can be evaluated through the spatial and temporal evolution of DNA double-strand breaks [Sch10].

Input to these and other issues could contribute to the further improvement of radiotherapy outcomes and consequently to the decrease of mortality rates in cancer patients.

In this work we study the viability of implementing an experimental setup at one of the beam lines of the 18-MeV proton cyclotron recently installed at Instituto de Ciências Nucleares Aplicadas à Saúde, University of Coimbra, Portugal. Such setup should allow radiobiological studies to be performed, including the effects of proton irradiation on cell cultures and small animals.

Several Monte Carlo simulations based on Geant4 were deployed to optimize the setup under study. These were initially validated with against packages such as SRIM/TRIM and also

against theoretical published results. Dose calculations were performed using different configurations to evaluate depth-dose profiles and dose 2D distributions.

Chapter 1

Radiotherapy With Protons

1.1 Motivation

Cancer is a major concern in today's society, as more than one in three people will have cancer during their lifetime [CRU10b]. Only in 2008 almost 13 million new cases of cancer were registered and almost 8 million people died all over the world due to this disease [Fer10]. Furthermore, about three-quarters of all cases of cancer are developed by people with 60 years and over who represent 10% of the total world population nowadays and are expected to represent 22% in 2050. This fact combined with the prospective of increase of life expectancy from the current 65 years to 76 years in 2050, means that the number of occurrences of cancer will be higher in the future, admitting that the current rates of incidence (age-standardized

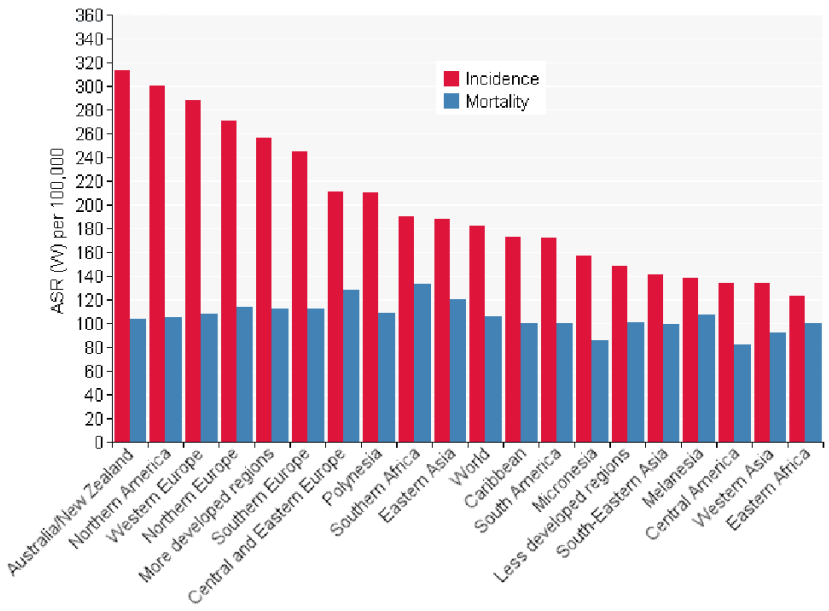

Figure 1.1: Cancer incidence and mortality rates per 100 000 population of both sexes and all ages in several regions of the world; after [Fer10]. Data for all types of cancer excluding non-melanoma skin cancer in age-standardized rates (ASR).

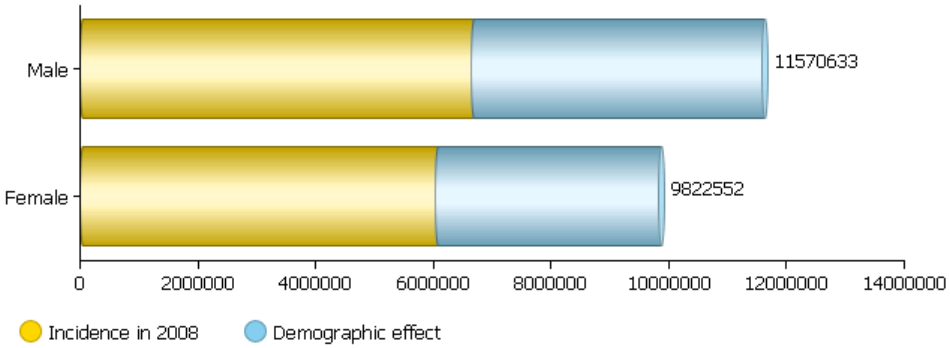

Figure 1.2: Prediction of the number of cases of cancer in 2030 for men and women of all ages worldwide. The prediction is performed by adding the expected demographic effect for the year 2030 to the number of cases of cancer registered in 2008; after [Fer10].

rates (ASR[1]) in Fig. 1.1) remain the same [CRU10a]. Fig. 1.2 shows a prediction of the number of cases of cancer in 2030 for men and women of all ages based on the numbers of 2008 and adding the expected demographic effect.

Looking at these statistics, specially at those concerning cancer mortality, one can realize how important it is to create and improve the existing conditions for people with cancer to have the highest probabilities of being cured or, at least, get palliative treatment. Radiotherapy plays a major role when it comes to cancer treatment, either curative or palliative. It can be administered alone or in a multimodality plan, usually in conjunction with surgery and/or chemotherapy. For example, in the United Kingdom 40% of the patients cured from cancer were treated with radiotherapeutical means [Boa03] and worldwide more than 50% of all cancer patients need to receive radiation therapy during their treatment [Boy08, Fow06, Sch06].

Radiotherapy has greatly improved since its early days, by the time of the discovery of the X-rays by Roentgen in 1895, and it is still in progress nowadays [Fow06]. All issues involved in treatment planning like patient positioning, dose calculation, tumor volume definition and localization, and the treatment technique are under constant research, so that the goal of radiotherapy can be fulfilled, i.e., to kill the tumor with the lowest possible damage to the surrounding healthy tissue [Sch06]. Furthermore, therapy with radiation is not limited to external beam radiation therapy (EBRT) and definitely not limited to photons and electrons. There are other options to consider such as brachytherapy, charged particle therapy, and neutron therapy, just to name a few. In particular, proton and carbon ion therapy are two topics of great interest nowadays. These particle techniques are characterized by a property not shared by photons and electrons, the Bragg peak, which allows for a higher deposition of energy in the target volume while lowering the dose to the vicinity. This characteristic may allow improving cancer treatment results, thereby contributing to the reduction of the mortality rates due to cancer.

[1] An age-standardized rate is a summary measure of the rate that a population would have if it had a standard age structure [Fer10]. The ASR is a weighted mean of the age-specific rates; the weights are taken from population distribution of the *standard population*. The most frequently used standard population is the *World Standard Population*. The calculated incidence or mortality rate is then called age-standardized incidence or mortality rate (world). It is also expressed per 100 000.

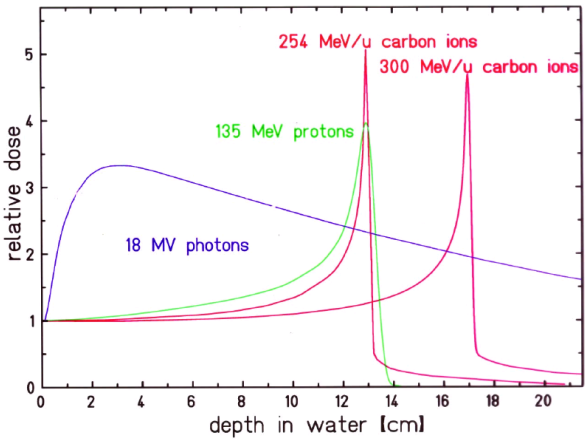

Figure 1.3: Depth-dose profiles for photons, carbon ions and protons; from [Lag07].

1.2 Brief history

Protons and heavier ions[1] were suggested as a possibility for radiation treatment for the first time in 1946, by Robert Wilson [Wil46], who thought that the depth-dose distribution presented by these particles would be adequate to treat tumors in humans. Unlike photons and electrons, these particles show a low and nearly flat energy deposition which increases with the penetration depth until it reaches a maximum called the Bragg peak, and then falls steeply to approximately zero (Fig. 1.3). This means protons and heavier charged particles will cause, towards the end of their range, higher ionization than photons or electrons of comparable energy, enabling the delivery of a higher dose to a deep-seated tumor, while sparing the surrounding healthy tissues. Protons, because distal to the tumor the energy deposition falls to zero, delivers no dose beyond the tumor [Kra00, Smi06]. Carbon and other heavy charged particles show an increased relative biological effectiveness (RBE) that potentiates their action mainly in the Bragg peak, in addition to a smaller lateral scattering and range straggling [Kra00].

Wilson also proposed a technique widely used today to encase all the volume of large tumors, using a range modulation wheel to produce a spread-out Bragg peak (SOBP). In Fig.1.4 we can see a SOBP built up from several pristine[2] Bragg peaks.

As soon as 1954, radiotherapy with protons started to be an option available to cancer patients at the Lawrence Berkeley National Laboratory (LBNL) [Tob58]. After some previous animal experiments [Tob52, Tob42] Tobias and his colleagues irradiated the first patient for a pituitary treatment with proton beams from the '184- inch Synchrocyclotron' built by Lawrence and Edlefsen in 1930 [Law30]. By 1957 radiotherapy with protons commenced in Europe at the University of Uppsala in Sweden, where a broad spectrum of cancers were treated, such as glioblastoma multiforme, carcinomas of the cervix, nasopharynx, head and neck, among others [Fal62]. Larsson and his team were the first to implement Wilson's idea of modulating the proton beam and producing a SOBP by designing the adequate ridge filters and they also were the first to use beam scanning to produce large treatment fields in the lateral dimension [Lar61]. Other proton therapy facilities were implemented in several countries like Russia (Dubna, 1967), Japan (Chiba, 1979), and Switzerland (Villigen, 1984) [Sui07, Smi06] in the following 30 years after the irradiation of the first patient at LBNL. Proton therapy has grown

[1] Ions heavier than protons are called *heavy* in radiobiology, as opposed to nuclear physics terminology, due to their increased biological effectiveness [Kra00].

[2] A pristine Bragg peak is the one measured for a single energy beam [She08].

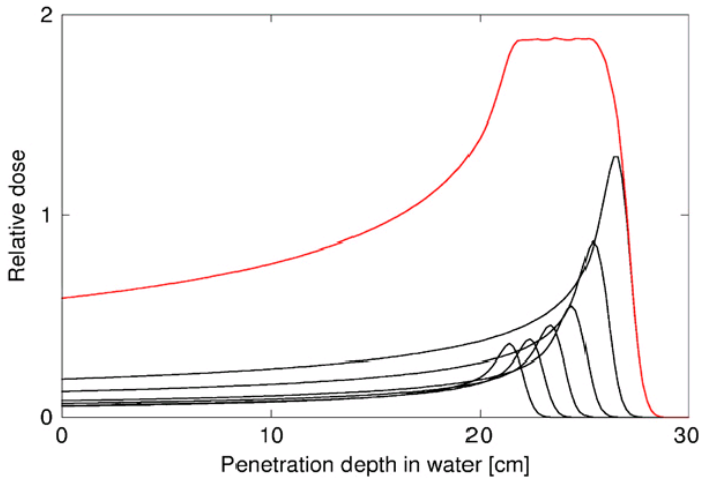

Figure 1.4: Spread-out Bragg peak (SOBP) produced from several pristine Bragg peaks through range and intensity modulation. SOBPs can be achieved using a physical device (ridge filter or modulation wheel) or selecting the energy from the accelerator and weighting each individual Bragg peak; from [Smi06].

significantly with about 67 000 patients treated to date worldwide [Jer10]. Table 1.2 lists all centers in operation in 2010.

1.3 Rationale

When we refer to the rationale for using protons in radiotherapy we are evoking both the physical rationale and the radiobiological rationale. The former has to do with the physical processes that occur when the proton interacts with matter in general, and the latter pertains to the reactions (and its consequences) at a cellular level.

1.3.1 Physical rationale

As previously mentioned in section 1.2, protons were considered an option to radiotherapy due to their depth-dose profile [Wil46]. This profile, the Bragg curve, shows a narrow peak near the end of the particles track, which makes protons suitable for the treatment of deep-seated, inoperable, radioresistant, and/or close to organs at risk (OAR) tumors. This characteristic profile is explained by protons interaction with matter, which at this energy level are known to be mainly Coulomb interactions with bound atomic electrons. This electronic energy loss is described by the Bethe-Bloch equation (equation 1.1), which gives the mean rate of energy loss (or stopping power) [Nah07a, Kra00, Nak10]:

$$-\frac{dE}{dx} = Kz_{eff}^2 \frac{Z}{A}\frac{1}{\beta^2}\left[\frac{1}{2}\ln\frac{2m_e c^2\beta^2\gamma^2 T_{max}}{I^2} - \beta^2 - \frac{\delta}{2}\right] \tag{1.1}$$

where T_{max} is the maximum kinetic energy that can be imparted to a free electron in a single collision. The other quantities are defined in Table 1.2.

Table 1.1: List of all currently operating proton therapy facilities; adapted from [pFa10].

Who, Where	Country	Max. Clinical Energy, MeV	Beam Direction	Start of Treatment	Total Patients Treated
ITEP, Moscow	Russia	250	horiz.	1969	4162
St.Petersburg	Russia	1000	horiz.	1975	1353
PSI, Villigen	Switzerland	72	1 horiz.	1984	5300
Dubna	Russia	200****	horiz.	1999	595
Uppsala	Sweden	200	1 horiz.	1989	929
Clatterbridge	England	62	1 horiz.	1989	1923
Loma Linda	CA.,USA	250	3 gantry, 1 horiz.	1990	14000
Nice	France	65	1 horiz.	1991	3935
Orsay	France	200	2 horiz.	1991	4811
iThemba Labs	South Africa	200	1 horiz.	1993	511
MPRI(2)	IN.,USA	200	2 gantry, 1 horiz.	2004	890
UCSF	CA.,USA	60	1 horiz.	1994	1200
TRIUMF, Vancouver	Canada	72	1 horiz.	1995	145
PSI, Villigen**	Switzerland	250*	1 gantry	1996	542
HZB (HMI), Berlin	Germany	72	1 horiz.	1998	1437
NCC, Kashiwa	Japan	235	2 gantry	1998	680
HIBMC, Hyogo	Japan	230	gantry	2001	2382
PMRC(2), Tsukuba	Japan	250	gantry	2001	1586
NPTC, MGH Boston	USA	235	2 gantry, 1 horiz.	2001	4270
INFN-LNS, Catania	Italy	60	1 horiz.	2002	174
Shizuoka	Japan	235	gantry, horiz.	2003	852
WERC, Tsuruga	Japan	200	1 horiz.,vertical	2002	56
WPTC, Zibo	China	230	2 gantry, 1 horiz.	2004	977
MD Anderson Cancer Center, Houston***	USA	250	3 gantry, 1 horiz.	2006	1700
FPTI, Jacksonville	USA	230	3 gantry, 1 horiz.	2006	1847
NCC, IIsan	South Korea	230	2 gantry, 1 horiz.	2007	519
RPTC, Munich**	Germany	250	4 gantry, 1 horiz.	2009	78
ProCure Proton Therapy Center, Oklahoma City	USA	230	gantry, horiz.	2009	21
HIT, Heidelberg**	Germany	250	1 gantry, 2 horiz.	2009	N.A.
UPenn, Philadelphia	USA	230	4 gantry, 1 horiz.	2010	N.A.

* degraded beam for 1996 to 2006; dedicated 250 MeV proton beam from 2007 on
** with beam scanning
*** with spread beam and beam scanning (MD Anderson, since 2008)
**** degraded beam
N.A. not applicable (treatment started)

Table 1.2: Quantities relevant for the Bethe-Bloch equation and some of their values according to [Nak10].

Symbol	Definition	Units or value
$\frac{dE}{dx}$	energy loss	$\mathrm{MeV\,g^{-1}\,cm^2}$
A	atomic mass of medium	$\mathrm{g\,mol^{-1}}$
N_A	Avogadro's number	$6.022\,136\,7(36) \times 10^{23}\,\mathrm{mol^{-1}}$
$\frac{K}{A}$	$4\pi N_A r_e^2 m_e c^2/A$	$0.307\,075$ MeV g^{-1} cm^2 for $A = 1$ g mol^{-1}
z_{eff}	effective charge of incident particle	
Z	atomic number of medium	
$m_e c^2$	electron rest energy	$0.510\,999\,06(15)$ MeV
I	mean excitation energy	eV
δ	density effect correction	

Most important in this equation is the dependence on $\frac{1}{\beta^2}$ and z_{eff}. These two are key factors to understand the appearance of protons Bragg peak near the end of their range, as emphasized in an energy loss versus depth plot. The $\frac{1}{\beta^2} \simeq \frac{1}{E}$ factor yields an increasing energy loss with decreasing particle energy, related to the time a given through-going particle is disturbing the atomic cloud; at low energies, in turn, not only the available energy is small, but electrons from the target are collected by the passing particle, thus rapidly decreasing its z_{eff}. The two contributions cause the distinct maximum of energy loss. Also, the low energy loss at higher energies explains the quasi constant plateau of energy deposition in the entrance [Kra00]. These characteristics can be seen in Figure 1.5 for several ions, with the stopping power displayed with units of linear energy transfer (LET), a measure of the energy deposited in the target by all electrons ejected by the passing particle.

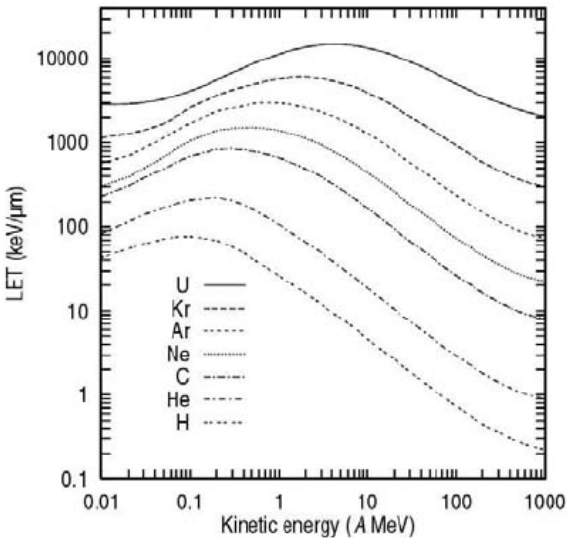

Figure 1.5: Energy loss in water for several particles; after [Sch91, Cre05]. The curves were calculated with the computer code ATIMA (atomic interactions with matter).

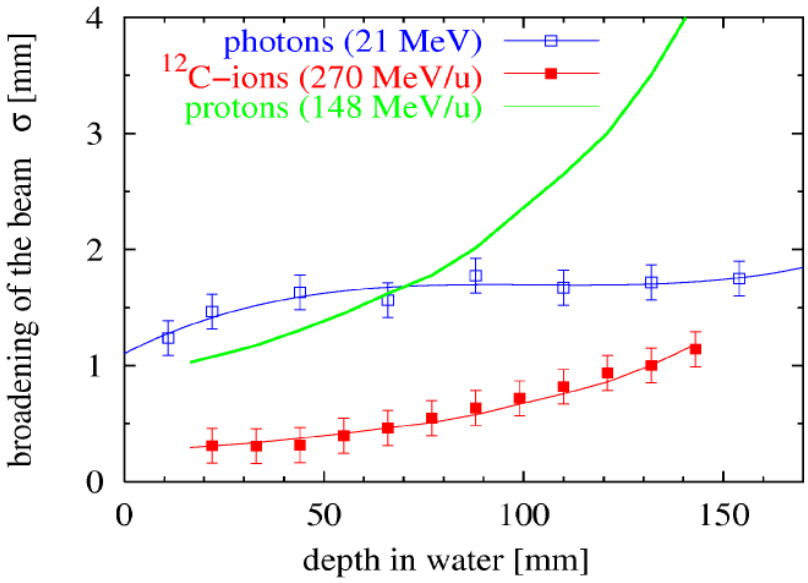

Figure 1.6: Lateral broadening of a photon, carbon and proton beam; after [Web96, Kra00].

Another relevant process is multiple Coulomb scattering (MCS). Protons suffer small angles deflections when traversing a medium due to both strong interactions and, mainly, Coulomb interactions with target nuclei. Coulomb scattering distribution is approximately Gaussian for small deflection angles, showing larger tails for larger angles [Nak10]. For small angles θ it is enough to use a Gaussian approximation with an angular width given by [Hig75, Kra00].

$$\sigma_\theta = \frac{14.1\,MeV}{\beta pc}\; z\; \sqrt{\frac{x}{X_0}\left(1 + \frac{1}{9}\log_{10}\frac{x}{X_0}\right)}, \tag{1.2}$$

where p is the momentum, βc the velocity, and z the charge of the projectile. $\frac{x}{X_0}$ is the thickness of the scattering medium expressed in radiation length[1].

MCS has consequences both on the lateral width (Fig. 1.6) and range straggling of proton beams (Fig. 1.3). In Fig. 1.3 the comparison between photon, carbon and proton beams shows that carbon has the lowest beam width and that for protons the lateral scattering exceeds the one of the photons for penetration depths larger than 7 cm. In Fig. 1.3 the smaller range straggling of carbons in comparison to protons can be observed.

Beam lateral scattering is very important from the clinical point of view, even more than the longitudinal scattering. That is because the treatment planning avoids the stopping of the beam in front of the OAR due to range uncertainties and, consequently, tumor volumes close to critical structures can only be irradiated with the beam passing by. The distance at which the beam will pass by is determined by its lateral scattering [Kra00].

There are several published proton multiple Coulomb scattering measurements, ranging from 1 MeV to 200 GeV of incident energy [Got93].

[1] Mean distance over which a high-energy electron loses all but $\frac{1}{e}$ of its energy by bremsstrahlung [Nak10].

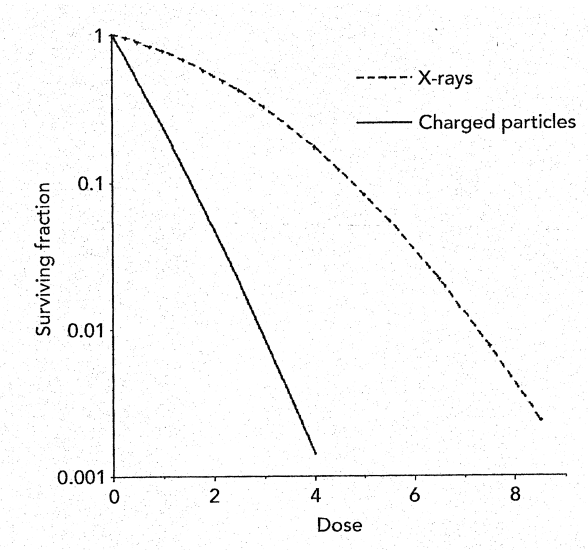

Figure 1.7: Characteristic cell survival pattern for low-LET X-rays and high-LET charged particles or neutrons; from [Ger07]. Higher LET radiations increase the slope of cell survival curve, resulting in a larger relative biological effectiveness per unit dose.

1.3.2 Radiobiological rationale

Radiation can cause damage in the tissues either by direct or indirect action. In direct action the radiation interacts directly with the critical target in the cell (mostly DNA), ionizing and exciting the atoms of the target through Coulomb interactions. This triggers a chain of physical and chemical events that may, or may not, lead to the biological damage [Sun05]. Indirect action occurs when the radiation interacts with other molecules and atoms within or in the surroundings of the cell, producing free radicals that diffuse until reach the critical target. In the case of indirect action, the radiation interacts mainly with water, in a process called radiolysis, from which results short lived but extremely reactive free radicals like $OH^{\cdot}$ (hydroxyl radical) [Sun05, For02].

Following the radiolysis of water other products are formed from subsequent reactions. For example, two $OH^{\cdot}$ can react forming H_2O_2 (hydrogen peroxide). This is quite relevant because $OH^{\cdot}$, along with H_2O_2, is responsible for approximately two-thirds of all radiation damage following the radiolysis of water [For02]. A known important factor that can enhance the radiation damage is the amount of oxygen in the tissues [Hal06].

Indirect action is very important when it comes to protons, because about two-thirds of the damage they induce is through this mechanism. This is true not only for protons but for all sparsely ionizing radiation or low-LET radiation [Sun05]. Photons, electrons, protons, and helium can be included in this category. Although protons are low-LET radiation and considered biologically radiation equivalent to photons [DK07], the resulting biological effects substantially differ, as shown in Fig. 1.7. The differences are due to the discrepancies in the relative biological effectiveness (RBE). The RBE is defined in reference to sparsely ionizing radiation, mostly 220 keV X-rays [ICR86, Kra00] and is the ratio of X-ray dose to particle dose that produces the same effect (Fig. 1.8). The effect may be cell killing, mutation, transformation, i.e., carcinogenesis, tissue damage, among other endpoints [Ger07].

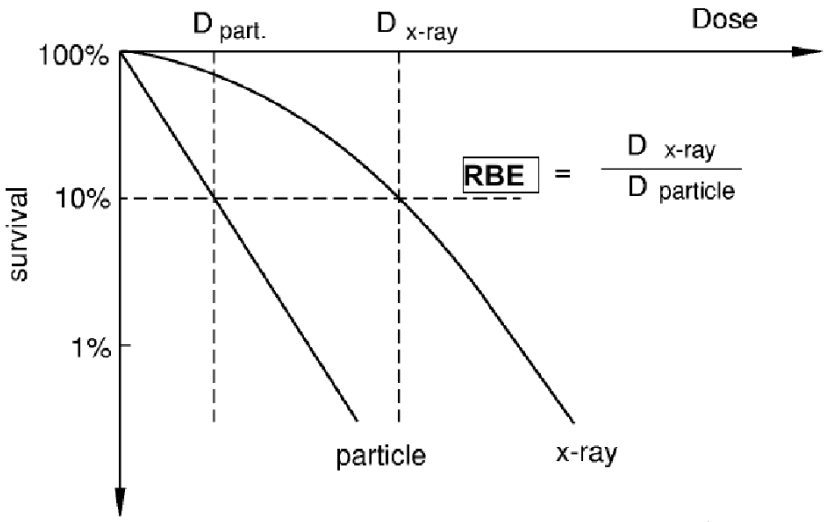

Figure 1.8: Definition of RBE, the relative biological effectiveness, illustrated with cell survival curves; from [Kra00].

For protons, there is evidence that the RBE increases slightly throughout the SOBP, specially in the distal one-third [Ger99, Raj95]. Carbon beams also present variations in the RBE along their track, but at a higher scale (section 1.4). RBE $>>$ 1 provides larger tumor-to-healthy tissue equivalent dosage, which potentiates useful clinical applications (section 1.5). So, this characteristic of protons can be seen as a drawback or as an advantage, depending on the therapeutical application in view. Although protons have a smaller biological effectiveness, this enhances simplicity of models for proton radiotherapy [Ger07].

1.4 Comparison with photons

The main advantage of protons, when compared with photons, is its inverted depth-dose profile, as depicted in Fig. 1.3. Unlike protons and heavier charged particles, photons depth-dose profile shows the highest energy deposition shortly after their entrance in the tissue, which then decreases exponentially as the penetration depth increases. Fig. 1.9 compares the irradiation of a young patient with medulloblastoma with conventional X-rays and protons. The differences are clearly visible, with the protons avoiding the irradiation of the OAR in the vicinity of the vertebral bodies.

Another important advantage of protons is that the beam can be driven by magnetic deflection, which permits directing and shaping the beam without any passive components (section 1.6).

The lateral scattering of protons can also be considered an advantage in comparison to photons, but only if the penetration depth does not exceed 7 cm (Fig. 1.6). Above that value, lateral scattering of protons increases very steeply.

The major hindrance to the further development of proton therapy is its relatively higher cost. It is estimated that the ratio of the costs of proton versus X-ray therapy per treatment fraction is about 2.4 [Pag06, Goi03].

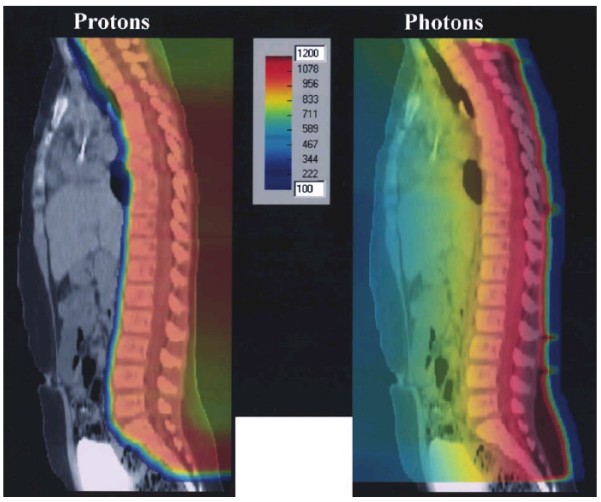

Figure 1.9: Treatment of a young patient with medulloblastoma; from [Sui03]. The image on the right side shows the irradiation with the conventional posterior 4 MV X-ray beam and resultant intermediate high dose to the anterior tissues/organs. The image on the left shows the treatment by a posterior proton beam which delivers nearly zero dose to all tissues anterior to the anterior surface of the vertebral bodies.

1.5 Comparison with other charged particles

Although protons share some features with heavy charged particles, such as the Bragg peak, some differences are also present. Even the Bragg peak shows dissimilarities between them, being narrower for heavy particles because they do not suffer as much Coulomb scattering from target nuclei as protons. However, heavy particles undergo a process called nuclear fragmentation [Nör80] that causes an increase in the dose beyond the Bragg peak, delivering unwanted dose distal to the tumor [Jäk06].

Heavy ions show an increasing RBE with increasing charge (Fig. 1.10). Carbon and neon ions, in particular, show a significant difference between the RBE at the entrance and at the Bragg peak, which allows for an enhanced dose essentially in the tumor, sparing the surrounding healthy tissues (Fig. 1.10 for carbon). In the particular case of carbon, the most studied heavy particle for therapy, with five currently operational centers in Japan, Germany, and USA [pFa10] and other five already proposed or under construction [pro10], the RBE values are between three and five at the Bragg peak for most radioresistant tumors [Cre05].

Because they are high-LET or densely ionizing radiation, heavy ions damage cells mainly through direct action. This is an enormous advantage because it eliminates the dependence on the presence of oxygen within the cell. Since the particles interact directly with the atoms of the cell, they cause unrepairable damage in the DNA whether there is oxygen or not [Cre05].

Another significant advantage of heavy ions is that they may interact with the target through a nuclear reaction , causing auto and/or target activation, and decay by β^+ decay [Cre05]. Fortunately, the positrons emitted allow monitoring the dose delivered to the patient with PET.

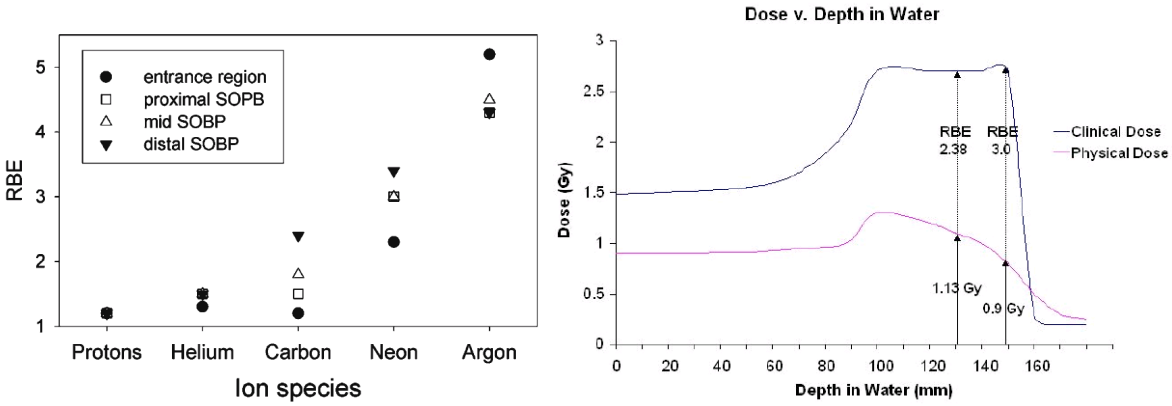

Figure 1.10: The RBE for a fractionated irradiation of jejunal crypt cells of mice after irradiation with different ions in different positions of a SOBP; from [Jäk06]. The modulation depth of the SOBP was 8-10 cm and the initial energy was 160, 225, 400, 557, and 570 MeV/u for protons, helium, carbon, neon, and argon ions, respectively. Proton data from [Tep77] and ion data from [Gol81] (left). Comparison between the physical and the biological dose for carbon ions; from [Kan99, Pag09] (right).

1.6 Equipment and facilities

The currently operating proton therapy centers are listed in Table 1.2. Some of them are hospital-based facilities (e,g., Loma Linda, USA), others are associated physically with a national laboratory (e.g., GSI, Germany), and others are stand-alone facilities not physically linked to any hospital (e.g., Orsay, France) [Tso07]. Nevertheless, all of them need an accelerator to produce the proton beams and adequate systems to perform the treatment delivery to the patient. These topics will be discussed in this section, along with the techniques more commonly used in proton therapy.

1.6.1 Accelerators

The accelerator used in a proton facility can be either a cyclotron or a synchrotron. A cyclotron is a circular chamber with two 'dees' acting like accelerating electrodes, while a magnetic field keeps particles in a circular trajectory with crescent radius. Beam particles are injected in the center of the cyclotron and then accelerated each time they pass through the electric field. When the beam reaches its maximum energy it is extracted from the cyclotron and directed to the treatment room. A synchrotron is a narrow vacuum ring tube that receives and accelerates a beam, generally pre-accelerated by a LINAC. The main difference to the cyclotron is that the synchrotron gradually increases the magnetic field to keep the beam within the tube as its energy also increases. The beam is extracted when the desired energy is reached, i.e., the synchrotron allows for energy variation [Fla07, Pag06].

Within a facility, an accelerator is generally used to serve more than one treatment room (Fig. 1.11). Clinical parameters such as dose rate, range, distal fall-off, and lateral penumbra are directly affected by the beam current, beam energy, the beam energy spread, and the beam size, respectively. Therefore it is important to assure that the accelerator is optimized for production of the intended clinical beams and delivery modalities. For example, if passive beam shaping (section 1.6.2) is used, the clinical parameters are also influenced by the materials

used to modulate the beam, so adjustments to the accelerator beam parameters will eventually be needed.

With the growing interest in proton therapy, there is the need of developing smaller cyclotrons that can be affordable to more medical centers. Since there is an evolution from therapy centers physically associated with a laboratory for physical research to hospital-based facilities, it is also needed that accelerators are designed according to this new reality. This should comprise, besides building more compact accelerators, designing equipment that allows for maintenance to keep a high reliability, investing in new methods of acceleration and improving treatment segments to allow more on-treatment adjustments to dose delivery, among other things.

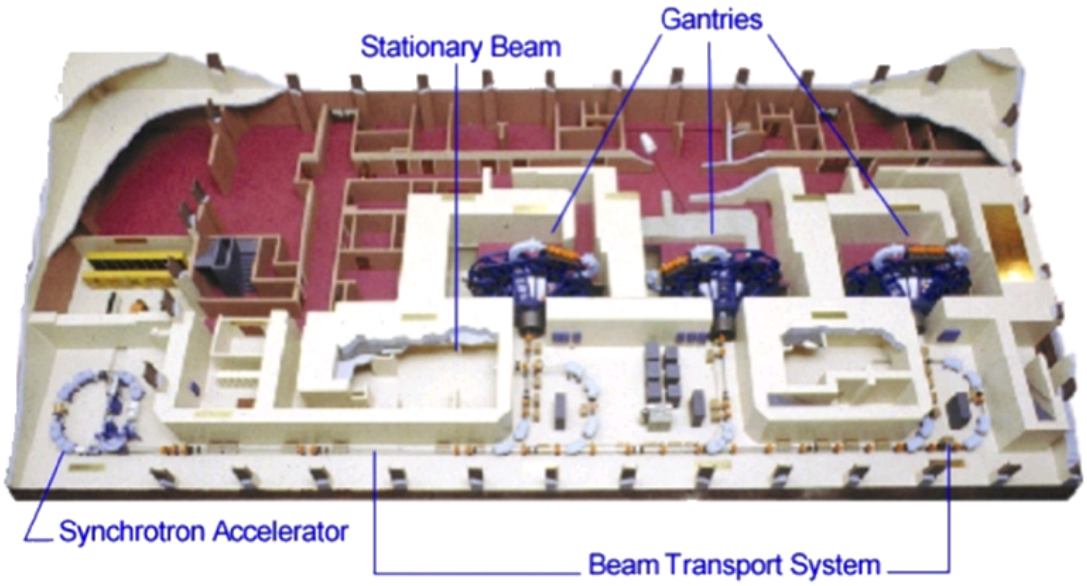

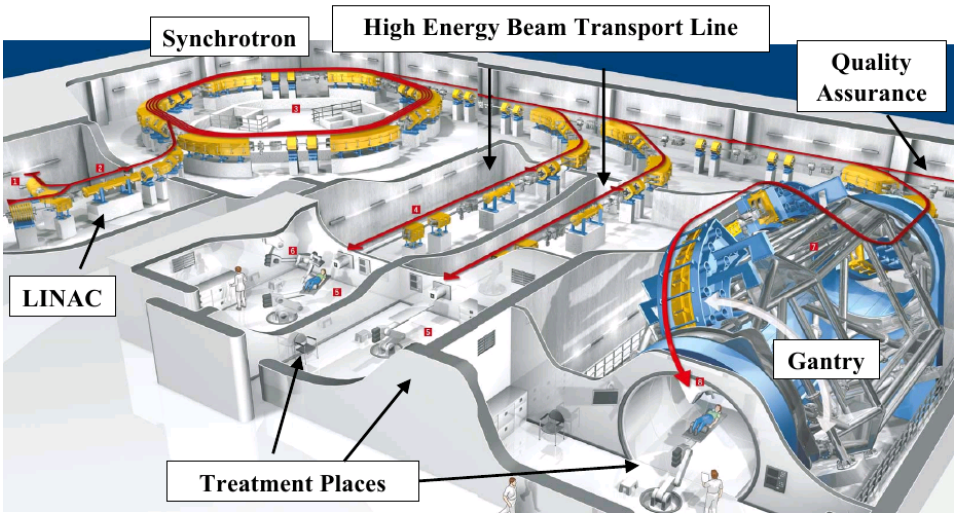

Figure 1.11: Floor plan of the Loma Linda University Medical Center's Proton Treatment Center, Loma Linda, CA, USA, with three gantry rooms and another with horizontal beams; from [Ama10]. The 7 m diameter synchrotron built by Fermilab accelerates the protons up to 250 MeV (top). Floor plan of the Heavy-Ion Therapy (HIT), Heidelberg, Germany, with one gantry room and two others with horizontal beams; from [Lag07] (bottom).

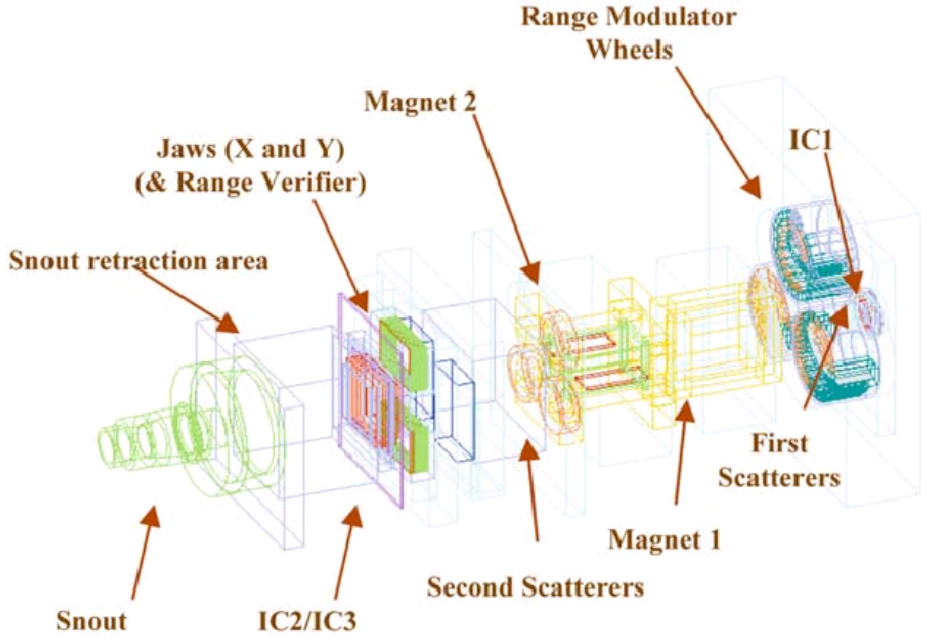

Figure 1.12: The nozzle at Francis H. Burr Proton Therapy Center, Boston, MA, USA; from [Pag04]. Beam monitoring devices are ionization chambers and a range verifier (multi-layer Faraday cup). Beam-shaping devices are scattering systems, range modulators, and wobbling magnets. Variable collimators ('jaws') and the snout determine the field size.

1.6.2 Treatment delivery systems

After the beam is extracted from the accelerator, it must be directed to the treatment rooms and to the patient. This is made through magnets for bending, steering and focusing. The treatment room can have either a fixed horizontal beam line or a full rotating gantry. The former allows only the irradiation of the patient in seated or near-seated positions, whereas the latter allows delivering the beam from any angle, which is of great importance when it comes to conformal radiation therapy. Gantries are quite large, typically with up to 10 m of diameter, for two reasons. First, protons at therapeutical energies require large radii to be bent, and second, they have to accommodate in their nozzle all the components for beam shaping and beam monitoring. Beam shaping devices include scatterers, absorbers, and other patient specific hardware [Fla07, Pag06]. Fig. 1.12 depicts the components of a nozzle in the Francis H. Burr Proton Therapy Center, formerly Northeast Proton Therapy Center (NPTC).

Passive beam shaping

Passive beam shaping and pencil beam scanning (or raster scanning) can be used to modulate the beam so it covers all the planning treatment volume (PTV). Passive shaping currently dominates clinical use because it is simpler to use than active systems (section 1.6.2), which use magnetic deflection to control the beam. In passive beam shaping the beam is spreaded out with scatterers to cover the field cross section. The SOBP is produced modulating the energy of the beam with range modulators like ridge filters, range-modulator wheels, and range shifters.

Additional modulation of the beam can be achieved using apertures and range compensators specific for each patient. Different combinations of these components are made in order to accomplish the desired dose distribution. However, care must be taken with the position (i.e., upstream or downstream) and the number of devices used, because there is the risk that dose sharpness is degraded and lateral penumbra augmented [Got07, Ped00, Pag06].

Another form of modulation can still be used with passive shaping, beam gating and current modulation. It consists, essentially in turning off the beam during part of the revolution, and varying the beam current during the modulator cycle, respectively, thereby reducing the high number of range modulators, apertures, and range compensators required to satisfy the needs of all patients [Got07].

Active beam shaping

Although it is still restricted to a few centers, the trend is towards the increase in the use of pencil beam scanning. Currently, only the PSI, the MD Anderson Cancer Center, the Francis H. Burr Proton Therapy Center, the RPTC, and the HIT have this technique available, but there are others already considering it [Nau10].

In pencil beam scanning, a narrow beam of protons is made to enter the patient at different locations by deflecting the beam under magnetic control. Although it is more complex, this avoids the considerably high number of devices utilized to modulate the beam with passive beam shaping, because it is usually applied without field- or patient-specific hardware, and under computer control. This brings other advantages like the reduction of the infrastructure for manufacturing and storing passive components, and the simplification of patient positioning, thereby diminishing the required treatment time. Also, the absence, or reduced number, of field-specific devices lowers the activation of the material near the patient [Ped00, Ped07].

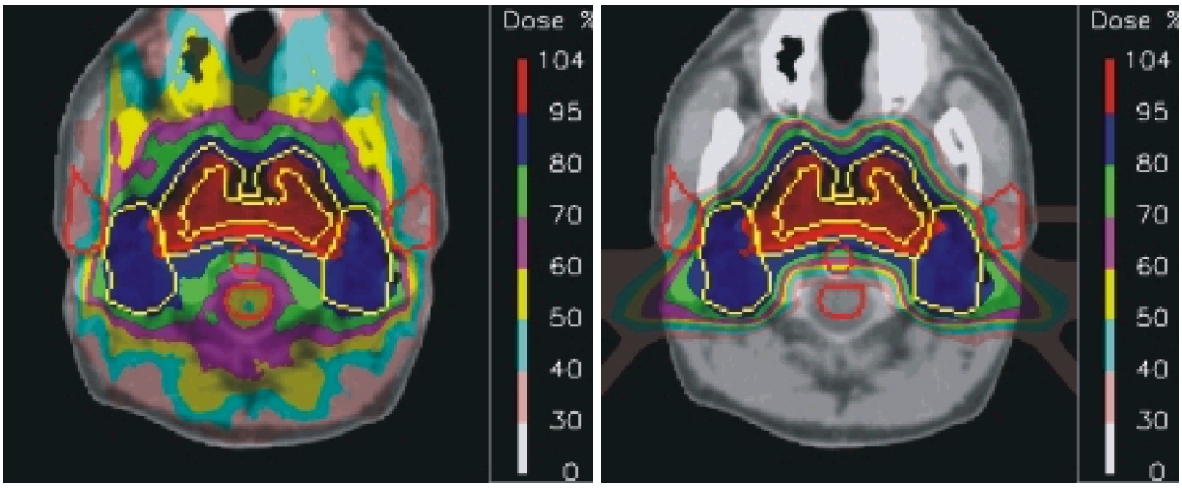

Figure 1.13: Example of intensity modulated therapy with photons (left) and spot scanning with protons (right); after [Ped00]. The yellow contours represent the targets (the visible tumor, the treatment volume with involved limph nodes). The red lines represent OARs to spare (salivary glands, brain stem). The dose distribution for photons (shown with color shading in percentage of the dose) is obtained through the superposition of 9 convergent photon fields. The dose distribution for protons is obtained this time with only 4 fields. The advantage compared to photons is the reduction of the dose outside the target volume.

Beam scanning manages to achieve a true 3D conformal dose distribution, conforming to the lateral, distal, and, in contrast to passive shaping, to proximal dimension of the PTV, preventing the delivery of unwanted dose to healthy tissues. The major disadvantage of pencil beam scanning in comparison with passive shaping is its higher sensitivity to organ motion [Ped00, Ped07].

Beam scanning is a subset of and intrinsically promotes the delivery of intensity-modulated proton therapy (IMPT) fields, which is analogous to intensity-modulated radiation therapy (IMRT) for photons. In IMPT, a single field delivers an inhomogeneous dose and the final homogeneous target dose is achieved only with multiple fields. IMPT allows designing and delivering dose to PTVs with complex shapes, even with convexities and holes. [Ped07]. The difference for IMRT is that it is possible to vary the energy of each pencil beam in addition to its intensity [Pag06]. Fig. 1.13 shows the distinct dose distributions obtained with IMRT and IMPT.

A specific modality of pencil beam scanning is spot scanning, which consists in delivering dose only in specific static positions, i.e., the beam moves without delivering dose until it reaches a particular position where the dose is delivered [Ped07]. It is simpler to use than raster scanning but, in turn, irradiation with this technique requires a higher amount of time and it is error-prone due to difficulties in achieving a highly uniform dose.

Chapter 2

Simulation Tools for the Development of a Proton Radiobiological Setup

2.1 Geant4 and SRIM/TRIM

The code for this work was implemented using Geant4 (Appendix A) [Ago03, All06]. Geant4 is an acronym for geometry and tracking and is based on Monte Carlo. First validations of the code were made against SRIM/TRIM (Appendix A) [Zie08]. SRIM stands for stopping and range of ions in matter and it is a group of programs which calculate the stopping and range of ions [SRI10]. TRIM is an acronym for transport of ions in matter and a computer program also based on Monte Carlo that calculates the interactions of energetic ions with amorphous targets [Zie08].

2.2 Validation of Geant4

The code used in this work is based on a hadrontherapy example from Geant4 and it was developed by G.A.P. Cirrone, F. Di Rosa, S. Guatelli, and G. Russo from Laboratori Nazionali del Sud of the National Institute for Nuclear Physics, Catania, Italy, and National Institute for Nuclear Physics Section of Genova, Genova, Italy. It was created in May 2005.

We used several setups for validating our code. We wanted to make sure we would obtain trustable results with it. As that, we did one validation for proton range, and another for beam lateral scattering.

2.2.1 Proton range

The setup depicted in Fig. 2.1 was used for validation of proton range in water. The water target thickness was chosen based on a first calculation with SRIM, from which resulted a projected range of 3.45 mm. So we proceeded to the simulation of a 18-MeV proton beam hitting a 5-mm long water target. We used an ideal source and put both the target and the source within a spheric perfect detector so that particles eventually leaving the target could be detected. It is important to notice that the detector is in vacuum and not in air. This consideration was made for simplification reasons, as we are interested solely, in this case, in determining the proton range in water. Furthermore, SRIM/TRIM calculations are also

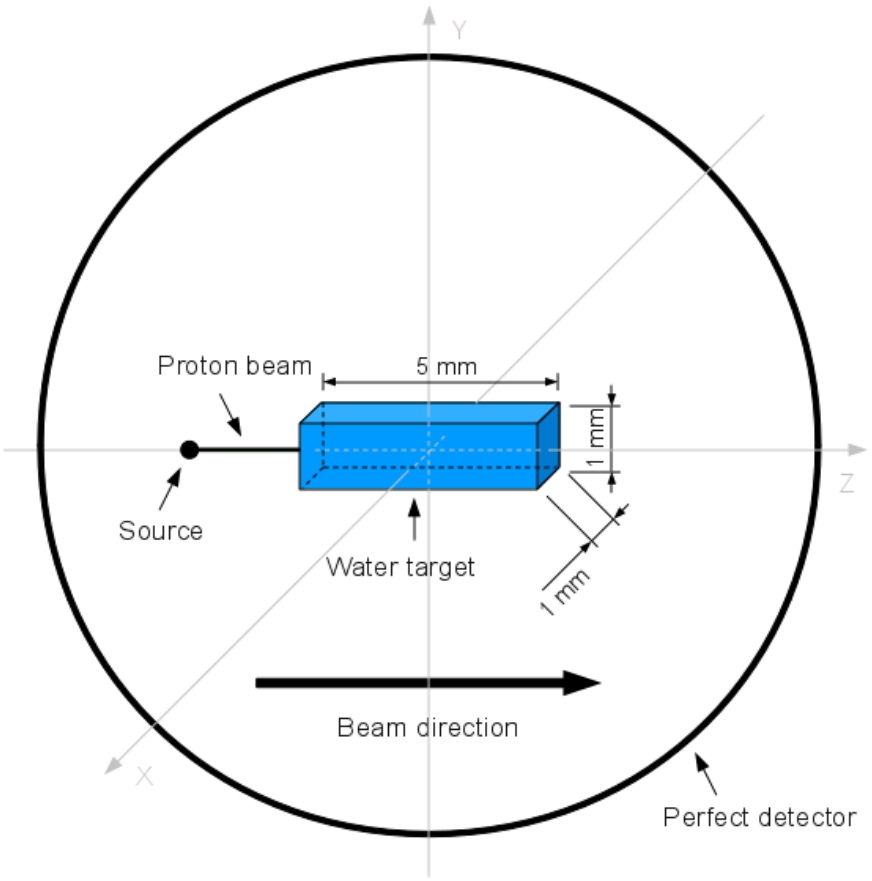

Figure 2.1: Schematic representation of the simulation setup used for proton range validation. A water target with dimensions 1x1x5 mm is in the center of a 300-mm radius spheric perfect detector in vacuum. The distance between the point source and the water target center is 160 mm. The beam travels along the Z positive direction.

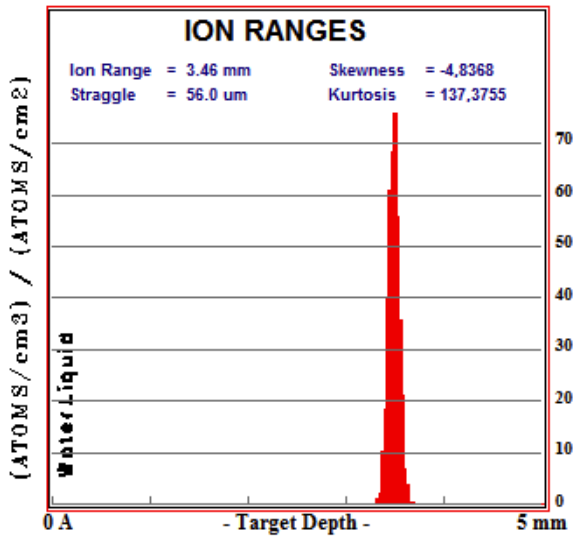

Figure 2.2: Range in water for 18-MeV protons, obtained using TRIM software. The simulation consisted in 99 999 pencil-beam shaped 18-MeV protons hitting a 5-mm long liquid water target with an angle of incidence of 0°.

idealized, considering that protons enter directly in the water target. So, vacuum is the most adequate 'medium' to compare simulation data of both SRIM/TRIM and Geant4.

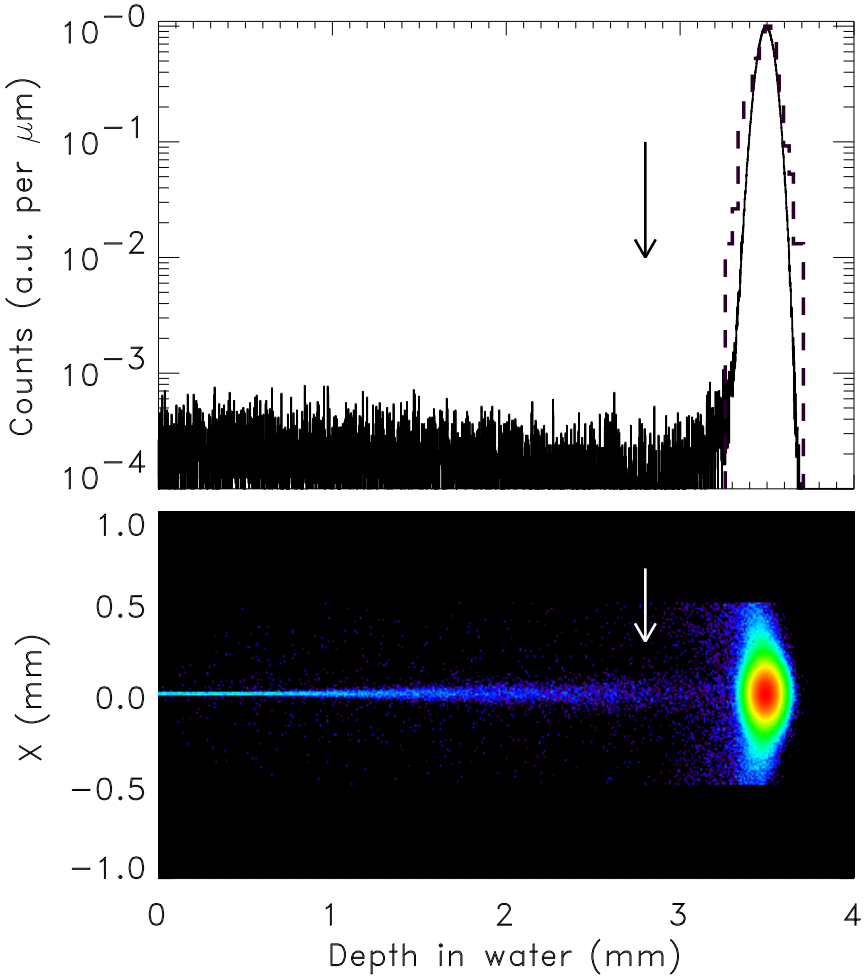

Figure 2.3: Range of 18-MeV protons in a 5-mm long water target. Top: depth profiles obtained with Geant4 (solid) and SRIM/TRIM (dashed). Bottom: Geant4-based 2D distribution. The Geant4 simulation consisted in 9 million pencil-beam shaped 18-MeV protons hitting the target in vacuum. The arrows point out the region where the energy of the projectiles falls below the Coulomb energy for collisions with target oxygen. Consequently, lateral straggling is highly enhanced passed this point.

Range validation was made against data obtained with TRIM. Fig. 2.2 shows the result of a TRIM simulation for 18-MeV protons range in water. These data were compared with Geant4 simulation outcome. The concordance between both curves can be observed in Fig. 2.3 (top), although Geant4 results show a higher number of particles that stopped at the entrance plateau before Bragg peak due to higher statistics (Geant4 was simulated with 9 million pencil-beam shaped protons and TRIM with only 99 999). The bottom graph of the Fig. 2.3 shows the resulting 2D distribution of protons in water from Geant4 simulation. It can be observed here, as well as in the top graph, a decrease in the number of particles that stopped just before the Bragg peak. This is due to the the decrease of protons energy below Coulomb energy for collisions. In consequence, passed this point, there is a significant increase in lateral scattering, which will be discussed in the next section.

2.2.2 Proton beam lateral scattering

The setup used for validation of beam lateral scattering is depicted in Fig. 2.4. The difference for the setup in Fig 2.1 is target thickness, which is 1.5 mm in this case. This thickness was chosen to allow protons to interact with the target long enough to suffer Coulomb scattering, and then leave the target, being detected in the spheric perfect detector. Once again, the source is a point source and the detector is in vacuum for simplicity reasons.

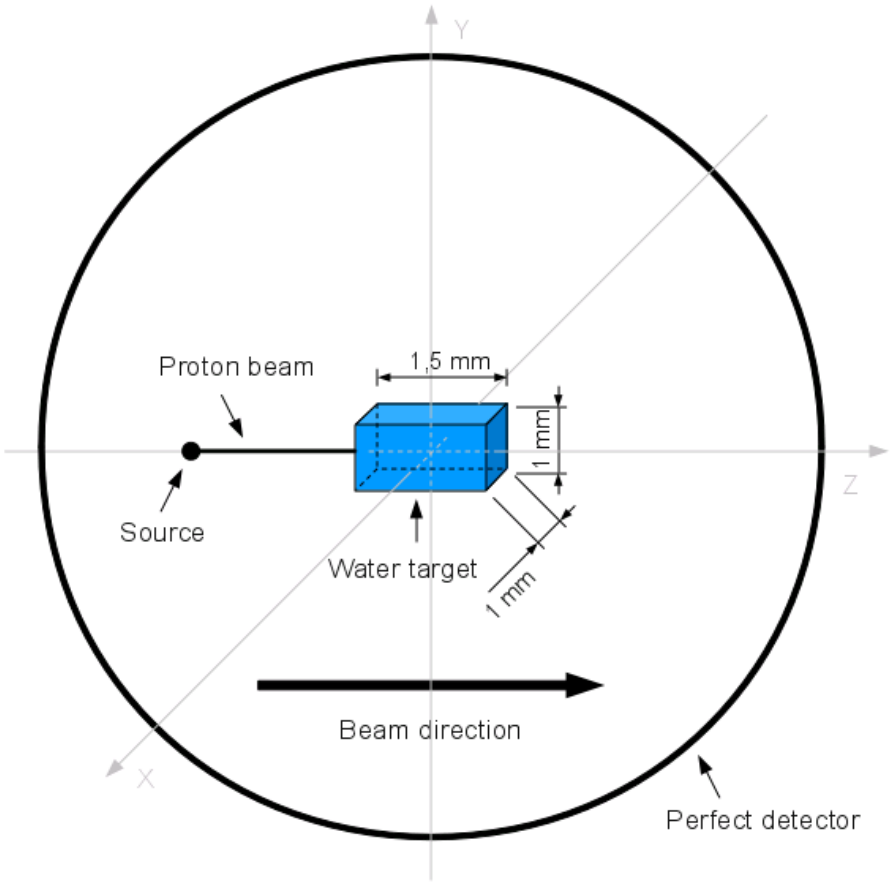

Figure 2.4: Schematic illustration of the simulation setup used for proton beam width validation. The water target with dimensions 1x1x1.5 mm is in the center of a 300-mm radius spheric perfect detector in vacuum. The distance between the point source and the water target center is 160 mm. The beam travels along the Z positive direction.

Validation is done against Equation 1.2. Values used for calculating σ_θ are listed in Table 2.1. $\frac{1}{X_0}$ for water is obtained summing the contributions from $\frac{1}{X_0}$ for oxygen and hydrogen (equation 2.1), yielding an equivalent value to tabulated X_0 for water, 36.08 g/cm^2.

$$\frac{18}{X_0(H_2O)} = \frac{2}{X_0(H)} + \frac{16}{X_0(O)}, \tag{2.1}$$

The theoretical value obtained for σ_θ was an angle of 1.2293°.

Table 2.1: Some of the values used for calculating beam lateral scattering.

Quantity	Value	Units
β	0.196815	
p	184.667485	MeV/c
c	299792458[a)]	m/s
z	1	
x	0.15	g/cm^2
$X_0(H)$	63.0470[b)]	g/cm^2
$X_0(O)$	34.2381[b)]	g/cm^2

[a)] According to [Nak10].
[c)] According to [Tsa74].

Data was fit with a pseudo-Voigt[1] function and the result corresponds to the blue curve in Fig. 2.5. The parameters used in the fit are listed in Table 2.2.2. The fit yielded a σ_θ value of $1.3678 \pm 0.0045°$ (338 iterations), which represents a difference of about 11.3% in respect to the theoretical value calculated.

Table 2.2: Parameters used to fit the simulated data to a pseudo-Voigt function.

Name	Value
ConstantG	80000
Mean	0
Sigma	1.35
Pedestal	0
Slope	0
ConstantL	-1500
Width	-2
Peak	4

This result may seem somewhat high, since dosimetry requires accurate outcomes. However, if we compare the theoretical value already calculated with the one obtained with another well-established expression, like equation 2.2 [Hig75, Hig79, Cre05], which yields a σ_θ of 1.0945°, a similar discrepancy can be observed. This value corresponds to a difference of nearly 10.9% in respect to the one calculated with equation 1.2. The reason for these uncertainties in σ_θ values obtained with both expressions can be explained by the fact that such expressions are obtained by adjustments made to beams with no negligible width.

$$\sigma_\theta = \frac{13.6\,MeV}{\beta pc}\; z\,\sqrt{\frac{x}{X_0}}\left[1 + 0.038\ln\left(\frac{x}{X_0}\right)\right], \tag{2.2}$$

[1] A Voigt function is the convolution of a Gaussian function and a Lorentzian function. As it requires a relatively involved computational procedure, it is often replaced by a pseudo-Voigt function, which consists in the weighted sum of a Gaussian function and a Lorentzian function [Ver06].

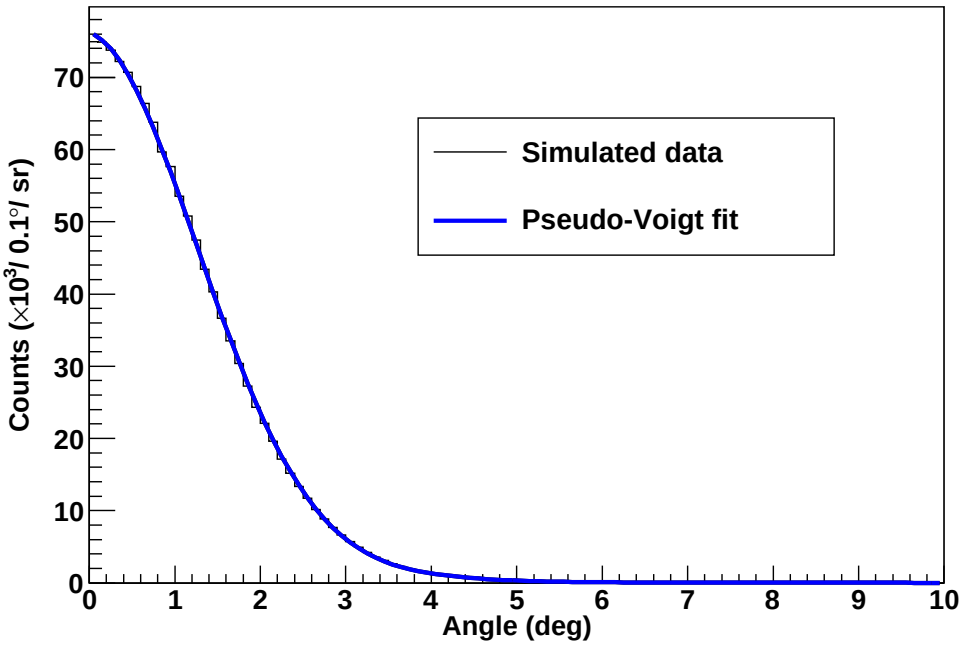

Figure 2.5: Proton beam lateral scattering. Angular distribution of 18-MeV protons after traversing 1.5-mm long water target. The simulation consisted in 25 million pencil-beam shaped protons hitting the target in vacuum.

Chapter 3

Concept for a Proton Cyclotron-Based Radiobiology Facility

Although it may be suitable for other cyclotron-based facilities, the setup described and studied in this work is planned to be implemented at one of the beam lines of the cyclotron recently installed at Instituto de Ciências Nucleares Aplicadas à Saúde (ICNAS), University of Coimbra. As that, it is important to know some of its features, which will be described briefly. The chronology of such information is also relevant in order to understand the sequence of this work.

After the first code validations, described in the previous chapter, what we will be doing here is a systematic approach with Geant4. We simulate the dose delivered by the cyclotron beam and study how dispersion influences it.

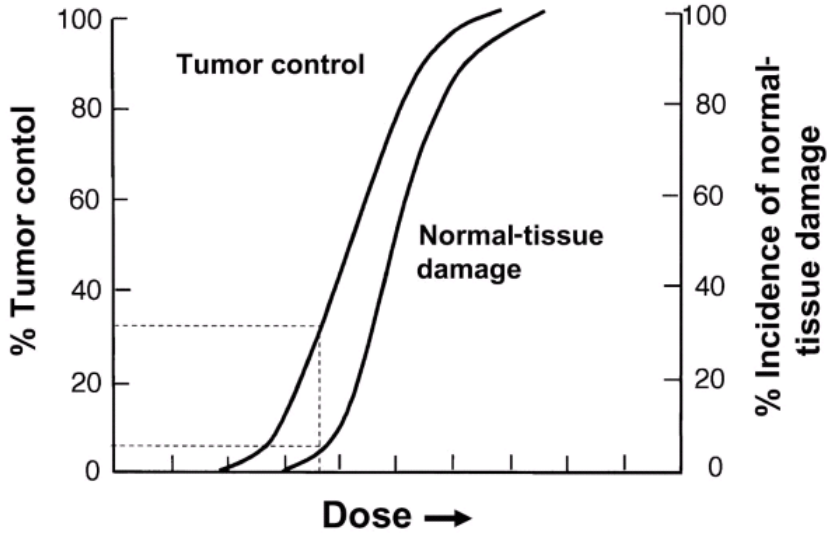

Figure 3.1: Dose-response curve for tumor control probability and normal tissue damage probability; from [Hal06]. The dose-response relationship is sigmoid in shape for both tumor control and normal tissue damage. That for normal tissue damage may be steeper than for tumor control. The therapeutic ratio (or index) is the percent of tumor control that can be achieved for a given level of normal tissue damage. In this hypothetical example, about 30% tumor control can be achieved for a 5% incidence of normal tissue damage.

The dose calculated in this work is the absorbed dose. Independently of the number of protons simulated, the depth-dose curves obtained correspond to the dose delivered by one million protons hitting the target. In radiotherapy, the accurate determination of this quantity is crucial due to the relatively steep sigmoidal dose-response curve for both tumor control and normal tissue damage (Fig. 3.1) [Nah07b]. Absorbed dose is a non-stochastic quantity applicable to both indirectly and directly ionizing radiations and is related to the stochastic quantity energy imparted. The absorbed dose is defined as the mean energy $\bar{\varepsilon}$ imparted by ionizing radiation to matter of mass m in a finite volume V by [Seu05, Nah07b, ICR80, ICR98]:

$$D = \frac{d\bar{\varepsilon}}{dm} \tag{3.1}$$

The energy imparted $\bar{\varepsilon}$ is the sum of all the energy entering the volume of interest minus all the energy leaving the volume, taking into account any mass-energy conversion within the volume. The unit of absorbed dose is joule per kilogram (J/kg). The name for the unit of absorbed dose is the gray (Gy).

3.1 ICNAS cyclotron

The cyclotron installed at ICNAS is manufactured by IBA (Ion Beam Applications, S.A., Belgium) and is a Cyclone® 18/9 HC, a fixed-energy cyclotron that accelerates protons and deuterons. Initial informations about beam energy were gathered in IBA's website, which indicates that protons are accelerated up to 18 MeV and deuterons up to 9 MeV [IBA10]. Later, in a private communication, we became aware of details about the beam port design, namely that it is composed of several materials, through which the beam has to pass before leaving the the cyclotron. The first one is a thin foil (approximately 50 μm) of Havar® (Appendix B) to keep the necessary low operating pressure inside the cyclotron; then, there is a chamber with gaseous helium that acts as a cooling system; in the other end of the chamber another material is placed, usually a thin foil (approximately 12 μm) of aluminum or titanium, to make the separation between the helium and the exterior of the cyclotron, to support the target and to act as a thermal interface between the helium and the target. In the context of the same private communication, a first approximation was made to what would be the beam dispersion, and the conclusions were that the beam would have a nearly Gaussian distribution with a FWHM (full width at half maximum) of 10 mm after 30 cm. Also, an estimed value was given for the beam energy after traversing these materials, which would be around 17 MeV for protons [Alv10a].

Through a contact with IBA Molecular, more precise specifications were obtained: the cyclotron is capable of accelerating protons up to 18.5 MeV and deuterons up to 9.2 MeV with beam currents equal to 150 μA and 40 μA, respectively; both beams present an approximately Gaussian distribution, with 80% of protons and 70% of deuterons within 10 mm and a dispersion of 3σ and 4σ, respectively; and the energy of the beam after leaving the port is 17.5 $\pm$ 0.2 MeV for protons and 8.2 $\pm$ 0.1 MeV for deuterons [Alv10b].

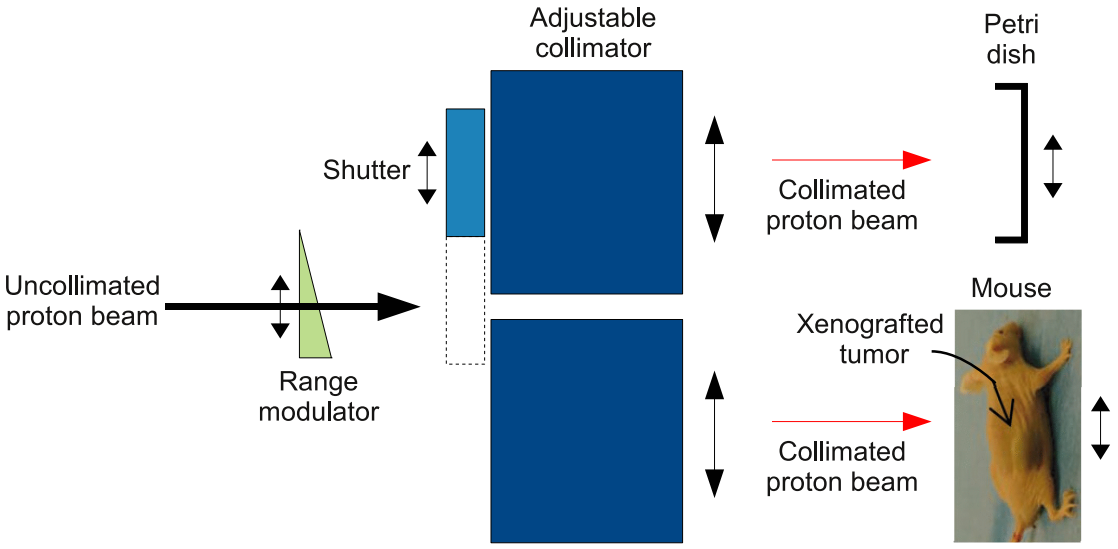

Figure 3.2: Concept of the experimental setup being planned at one of the beam lines of the cyclotron of the University of Coimbra. A moving range modulator allows for a controlled decrease in beam energy below 18 MeV. A shutter-equipped collimator with adjustable hole size follows. It regulates both beam lateral size and time exposure which, consequently, allows for the control of the area and dose delivered to the target. The target may consist of cell cultures, small animals, or dosimetric devices enabling the characterization and control of beam parameters.

3.2 Design proposal

Fig. 3.2 depicts the first draft of the experimental setup being planned, which will allow performing radiobiological studies either with cell cultures or small animals. It is composed of several devices, namely a moving range modulator, a shutter-equipped collimator, and a support system for the target. The range modulator permits decreasing the beam energy below 18 MeV; the collimator has an adjustable hole size, which permits controlling the area being irradiated; and the shutter associated with the collimator regulates time exposure and, thus, the dose delivered to the target.

3.3 Influence of beam divergence on dose delivery

3.3.1 Pencil beam

In a first phase of this study we did simulations with 18-MeV pencil-beam shaped protons hitting a water target, using the setup depicted in Fig. 2.1. The depth-dose profile in Fig. 3.3 is the one resulting from such simulation. It can be observed that the peak in this curve matches the simulated Bragg peak in Fig. 2.3, since it is verified at 3.449 mm. The dose at the peak is 2.9605 Gy.

Following this simulation, the next step was to introduce a small variation in water target density in order to study the influence of target density variation in depth-dose curves. This way we would be able to verify if and how such variation would affect the location of the peak into the target. Using the same setup (Fig. 2.1), but changing the water density from 1.00 g/cm^3

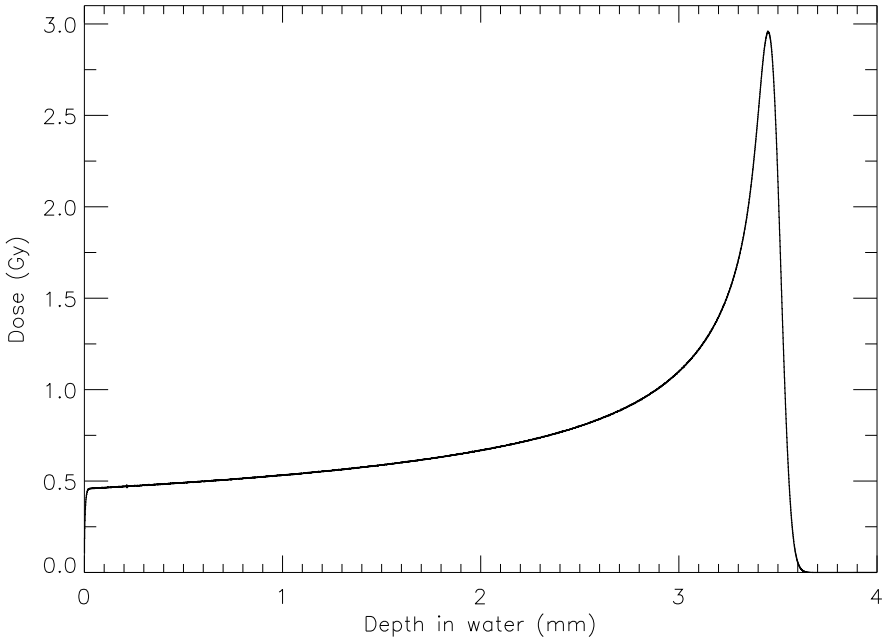

Figure 3.3: Depth-dose profile in water for 18-MeV protons. The curve peak is 2.9605 Gy for a depth in water of 3.449 mm. The simulation consisted in 9 million pencil-beam shaped 18-MeV protons hitting the target in vacuum.

to 1.05 g/cm^3, which means a difference of 5%, we obtained the depth-dose profile represented with a dashed blue line in Fig. 3.4(a). It can be observed that the curve peak is shifted to the left. It has now a value of 2.9619 Gy at 3.286 mm, which corresponds to a difference of 163 μm in respect to the solid black curve peak. When we were informed about the actual proton beam energy after leaving the beam port, 17.5 MeV, we used the same setup (Fig. 2.1) to make an identical simulation and determine the depth-dose profiles for protons with this energy. The resulting curves are shown in Fig. 3.4(b). In this case, the peaks are situated at 3.281 mm and 3.124 mm for the solid black line and the dashed blue one, respectively. The correspondent values of dose are 3.0189 Gy and 3.0234 Gy.

Fig. 3.5 compares the depth-dose profiles in water of regular density for 18-MeV and 17.5-MeV protons. It can be noticed that protons with less energy (dashed red line) have a smaller range in the same target.

In face of these results, we wanted to check if and with which proportions this phenomenon would occur for higher energies. So we made a simulation using the setup depicted in Fig. 3.6. The resulting dose profiles are shown in Fig. 3.6. Also in this case, it can observed that the peak of the depth-dose profile corresponding to the water target with 1.05 g/cm^3 is shifted to the left. The difference in this case is of 12.038 mm.

3.3.2 Beam with dispersion

After the private communication in which we were given a first approximation of what would be the beam dispersion [Alv10a], we started making simulations taking this variable in account. We calculated an angle of dispersion of 0.95484° for a FWHM of 10 mm at 30 cm. Also, we changed the beam energy to 17 MeV and considered a circular source with a radius of 1 mm.

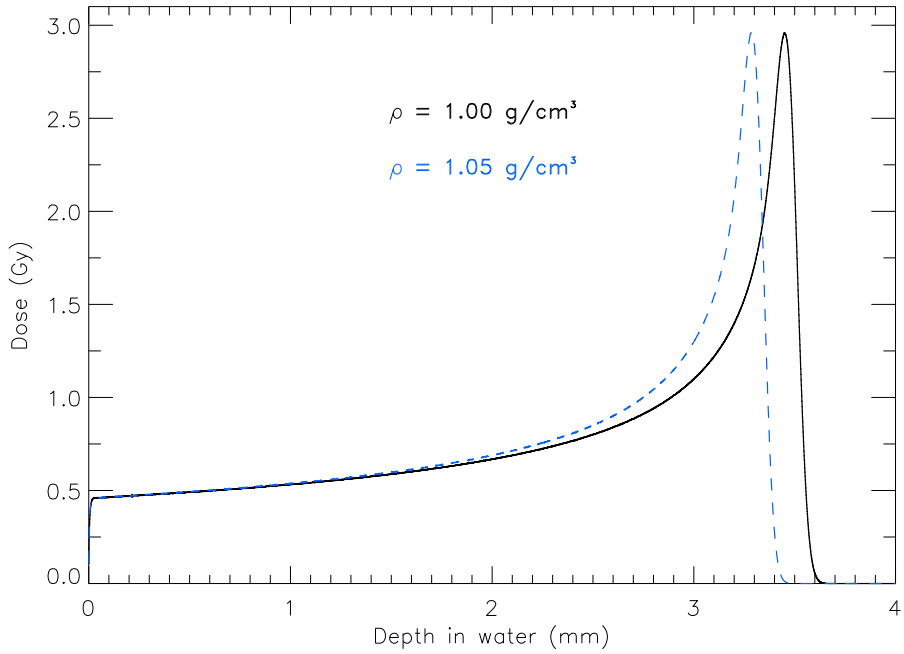

(a) 18-MeV protons.

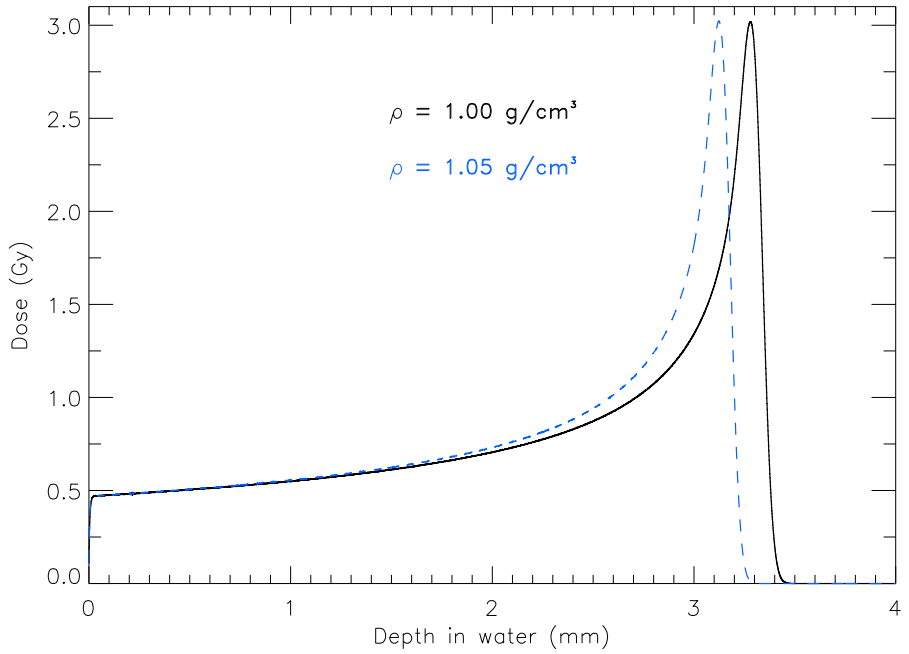

(b) 17.5-MeV protons.

Figure 3.4: Influence of density variation on depth-dose profile in water for 18-MeV and 17.5-MeV protons. The solid black curve is the depth-dose profile in water with a density of 1.00 g/cm^3 and the dashed blue one is the depth-dose profile in water with a density of 1.05 g/cm^3. The simulations to obtain these curves consisted in pencil beam shaped protons hitting the correspondent water targets with 5% difference in density. The total number of protons was 9 million for (a) and 8 million for (b). (a) The peak for the solid black curve is 2.9605 Gy at 3.449 mm and, for the dashed blue curve, it is 2.9619 Gy at 3.286 mm, which corresponds to a difference of 163 μm between both peaks. (b) The peak for the solid black curve is 3.0189 Gy at 3.281 mm and, for the dashed blue curve, it is 3.0234 Gy at 3.124 mm, corresponding to a difference of 157 μm between both peaks.

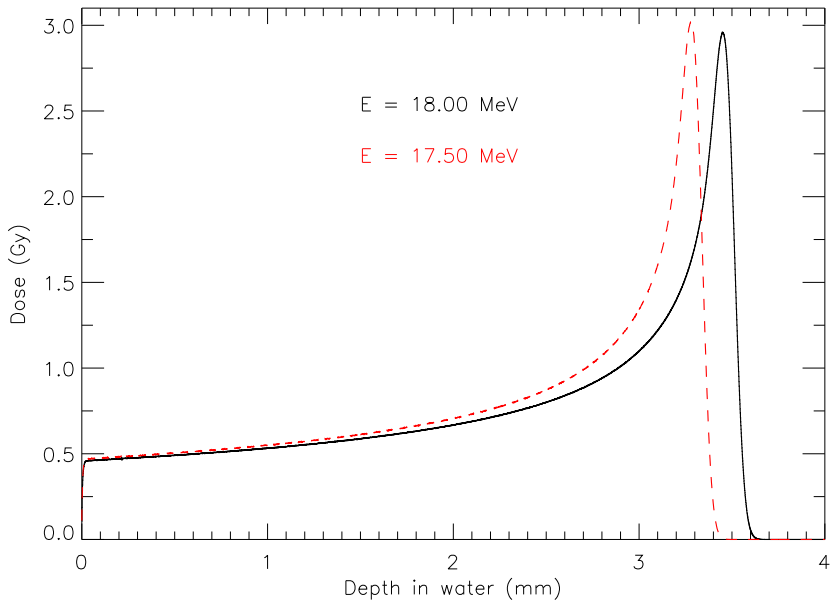

Figure 3.5: Influence of proton beam energy on depth-dose profile in water. The solid black curve represents the depth-dose profile in water for 18-MeV protons and the dashed red line corresponds to the same profile for 17.5-MeV protons. These curves are the same represented by the solid black line in Fig. 3.4(a) and (b), respectively.

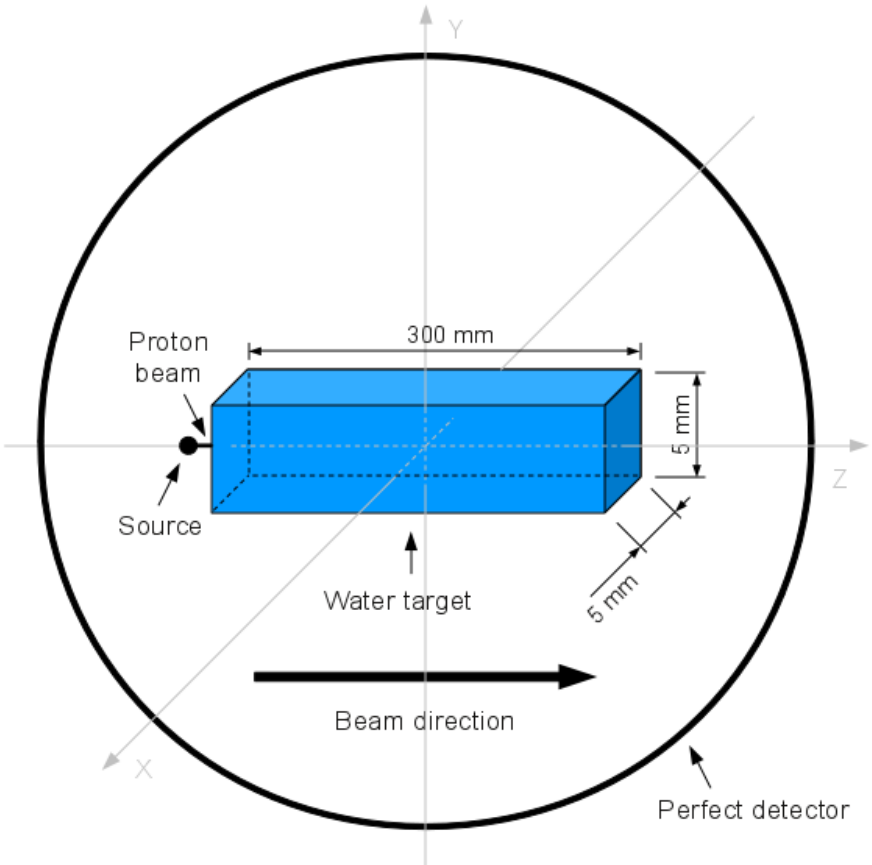

Figure 3.6: Schematic representation of the simulation setup used for irradiating water with 200-MeV protons. A water target with dimensions 5x5x300 mm is in the center of a 300-mm radius spheric perfect detector in vacuum. The distance between the point source and the water target center is 300 mm. The beam travels along the Z positive direction.

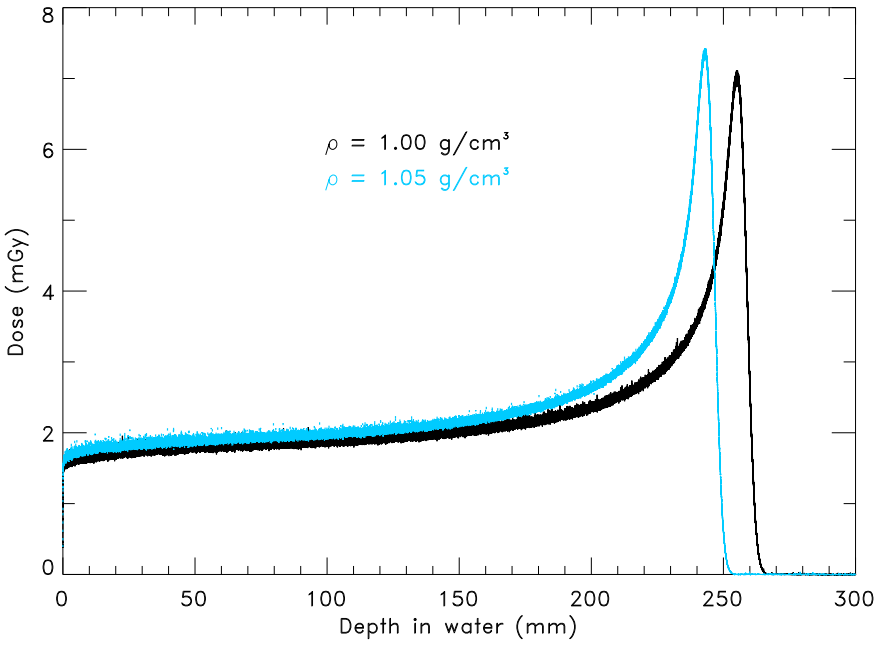

Figure 3.7: Influence of density variation on depth-dose profile in water for 200-MeV protons. The black curve is the depth-dose profile in water with a density of 1.00 g/cm^3 and the blue one is the depth-dose profile in water with a density of 1.05 g/cm^3. The peak for the black curve is 7.1170 mGy at 254.958 mm and, for the blue curve, the dose in the peak is 7.4487 mGy at 242.920 mm. This corresponds to a difference of 12.038 mm between both peaks. In both cases, the simulation consisted in 400 thousand pencil-beam shaped protons hitting a water target. The difference was the water density, which was 5% higher for the dashed blue curve.

Several setups were used for the simulations in this phase. We first simulated the effect of beam dispersion in a cylindric water target. The correspondent setup is represented in Fig. 3.8. The result is shown in Fig. 3.9(a). Looking at these curves one can see that the dose is higher within a radius equal to 1 mm and decreases as the radius increases, meaning that the dose is delivered mainly in the center of the target, even in the case of a beam with dispersion. Fig. 3.9(b) represents the same depth-dose profiles in the same target but for 17.5-MeV protons. This simulation was made after we were told the beam energy after traversing the material in the beam port is 17.5 MeV.

The following step was to study dose 3D distribution. We used the setup depicted in Fig. 3.10, in which there is a parallelepiped of dimensions 50x50x15 mm that is hit by protons. The dose in this target is registered in each 100 μm cube. The resulting 2D distribution from simulations with this setup, and the correspondent profile, is shown in Fig. 3.13.

Havar® target

At the time we got the information that the beam energy after leaving the beam port is 17.5 MeV, we were also informed that Havar® is the main responsible for beam dispersion [Alv10b]. As that, we used the setup depicted in Fig. 3.12 to study the influence of Havar® on dose. This setup uses the same source and beam dispersion considered in the previous case, but between the source and the target, at a distance of 300 mm from the source

and 150 mm from the water target, there is a 50-μm-long Havar® foil.

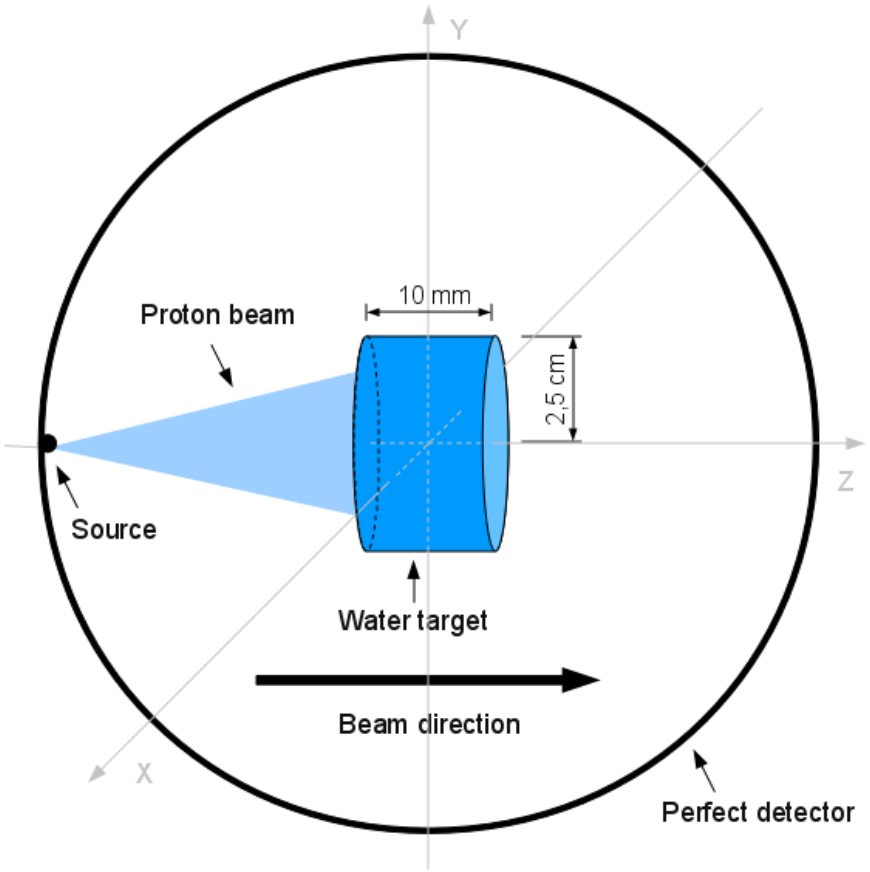

Figure 3.8: Schematic representation of the simulation setup used for first simulations of a beam with dispersion. A 25-mm radius and 10-mm long cylindric water target is in the center of a 300-mm radius spheric perfect detector in vacuum. The distance between the circular source and the water target center is 300 mm. The beam travels along the Z positive direction with 0.95484° dispersion.

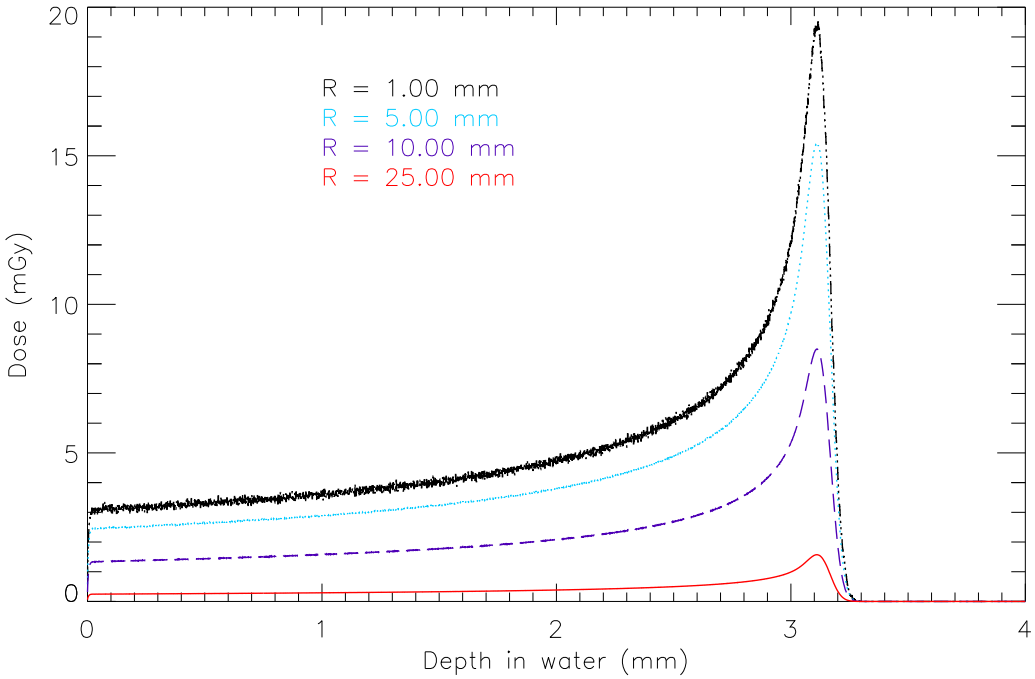

(a) 17-MeV protons.

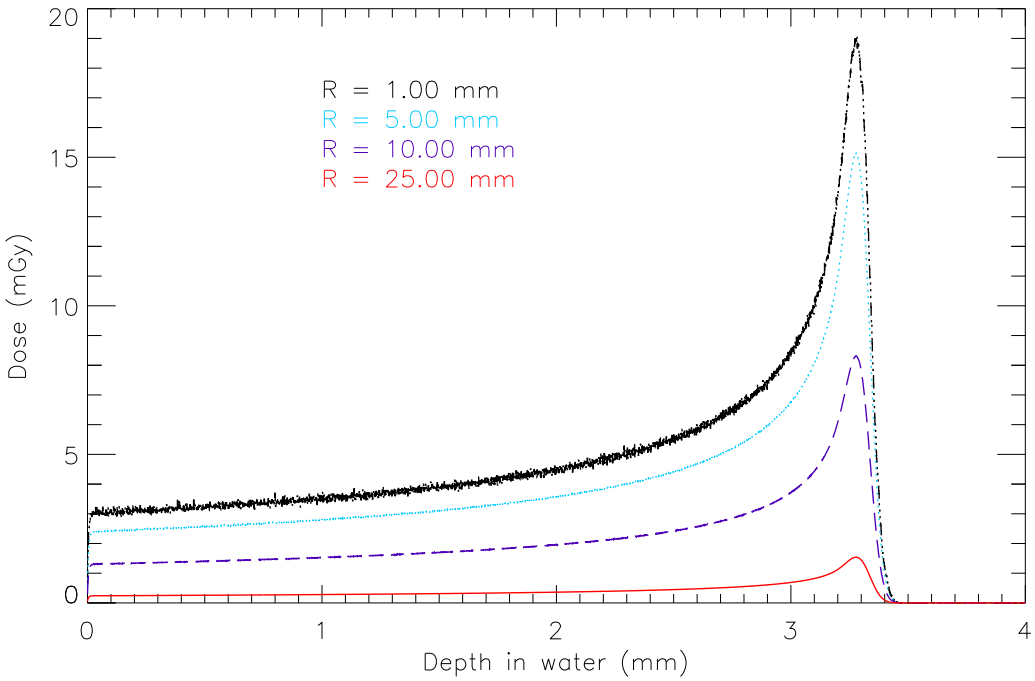

(b) 17.5-MeV protons.

Figure 3.9: Depth-dose profiles in water at four different radius for 17- and 17.5-MeV protons. The dotted dashed black line is the depth-dose curve for a 1-mm radius cylindric water target, the dotted blue line is the one for a 5-mm radius, the dashed purple line for a 10-mm radius and the solid red line for a 25-mm radius. The simulations consisted in 1 million pencil-beam shaped 17-MeV (a) and 17.5-MeV (b) protons with dispersion from a 1-mm radius circular source hitting 25-mm radius cylindric water target in vacuum.

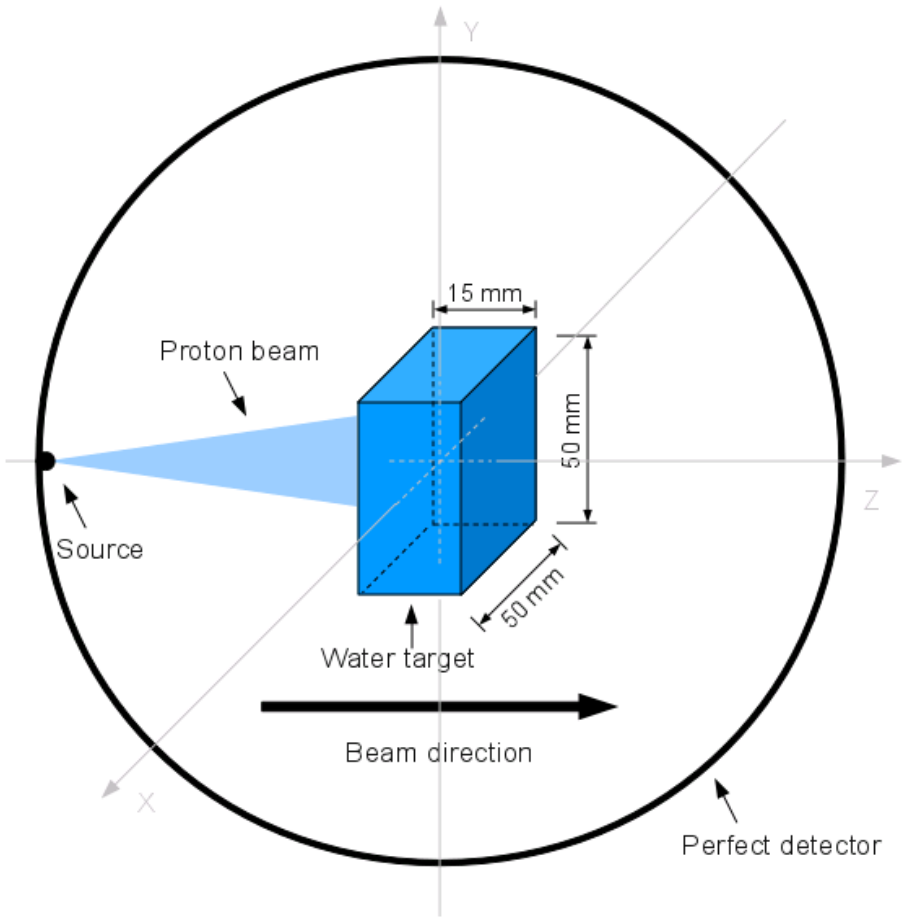

Figure 3.10: Schematic illustration of the simulation setup for calculating the dose 3D distribution. A water target with dimensions of 50x50x15 mm is in the center of a 300-mm radius spheric perfect detector in vacuum. The distance between the circular source and the water target center is 307.5 mm. The beam travels along the Z positive direction with 0.95484° dispersion.

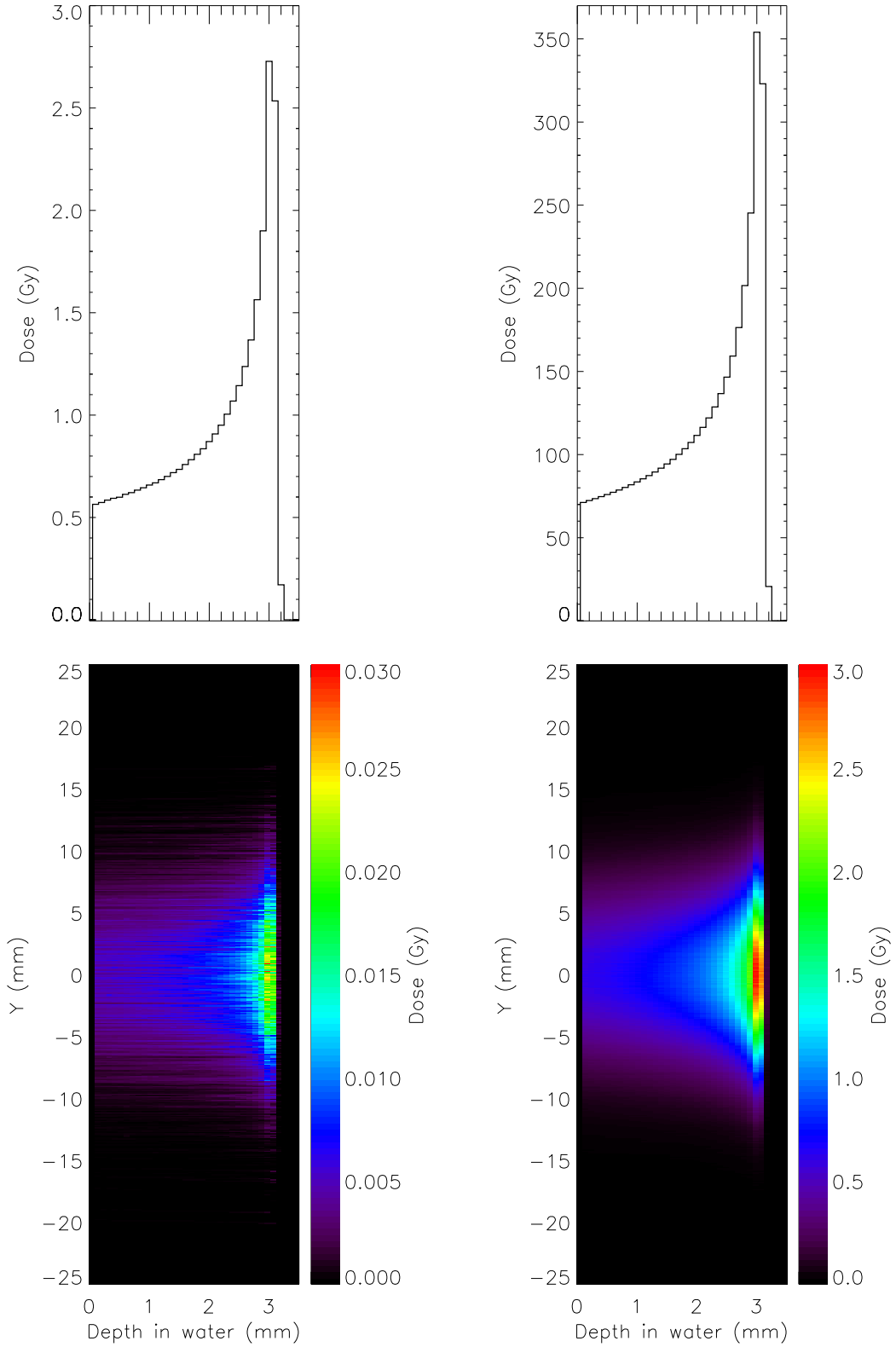

Figure 3.11: Depth-dose profile (top) and 2D distribution (bottom) of 17-MeV protons in water in the target central slice (left) and in the entire target (right).

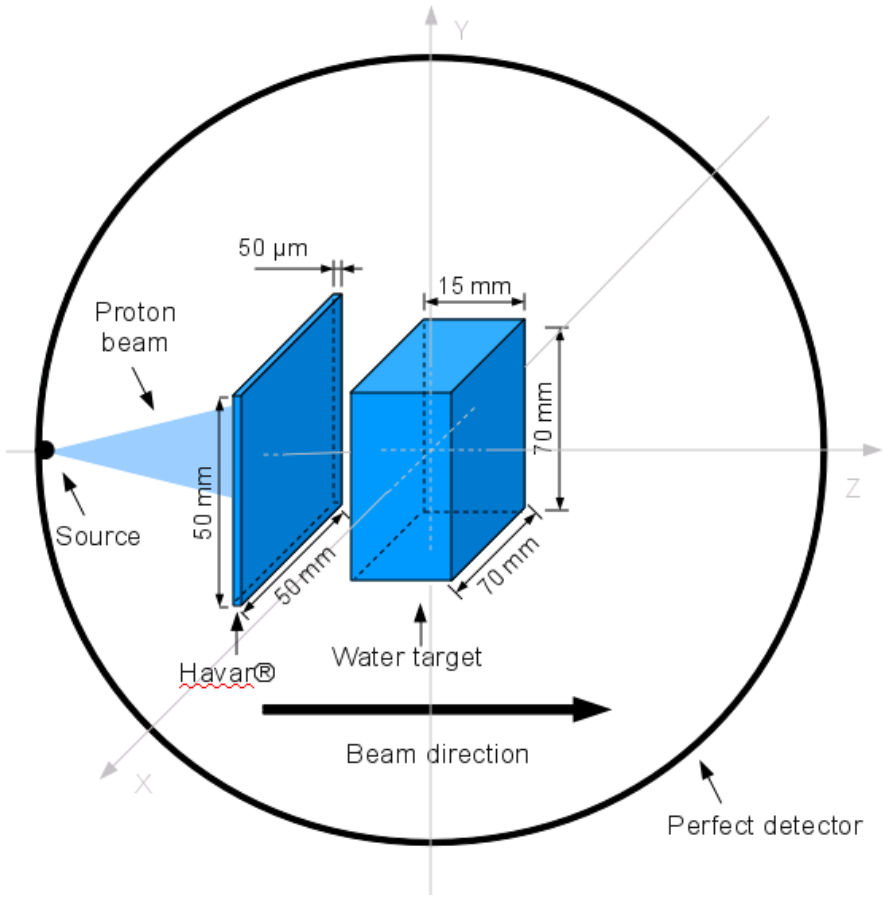

Figure 3.12: Schematic illustration of the simulation setup for studying the influence of Havar® on dose 3D distribution. A water target with dimensions of 70x70x15 mm is in the center of a 450-mm radius spheric perfect detector in vacuum. Between the source and the target there is a 50-μm-long Havar® foil. The distance between the circular source and the Havar® foil center is 300-mm. and the distance between the water target center and Havar® is 150 mm. The beam travels along the Z positive direction with 0.95484° dispersion.

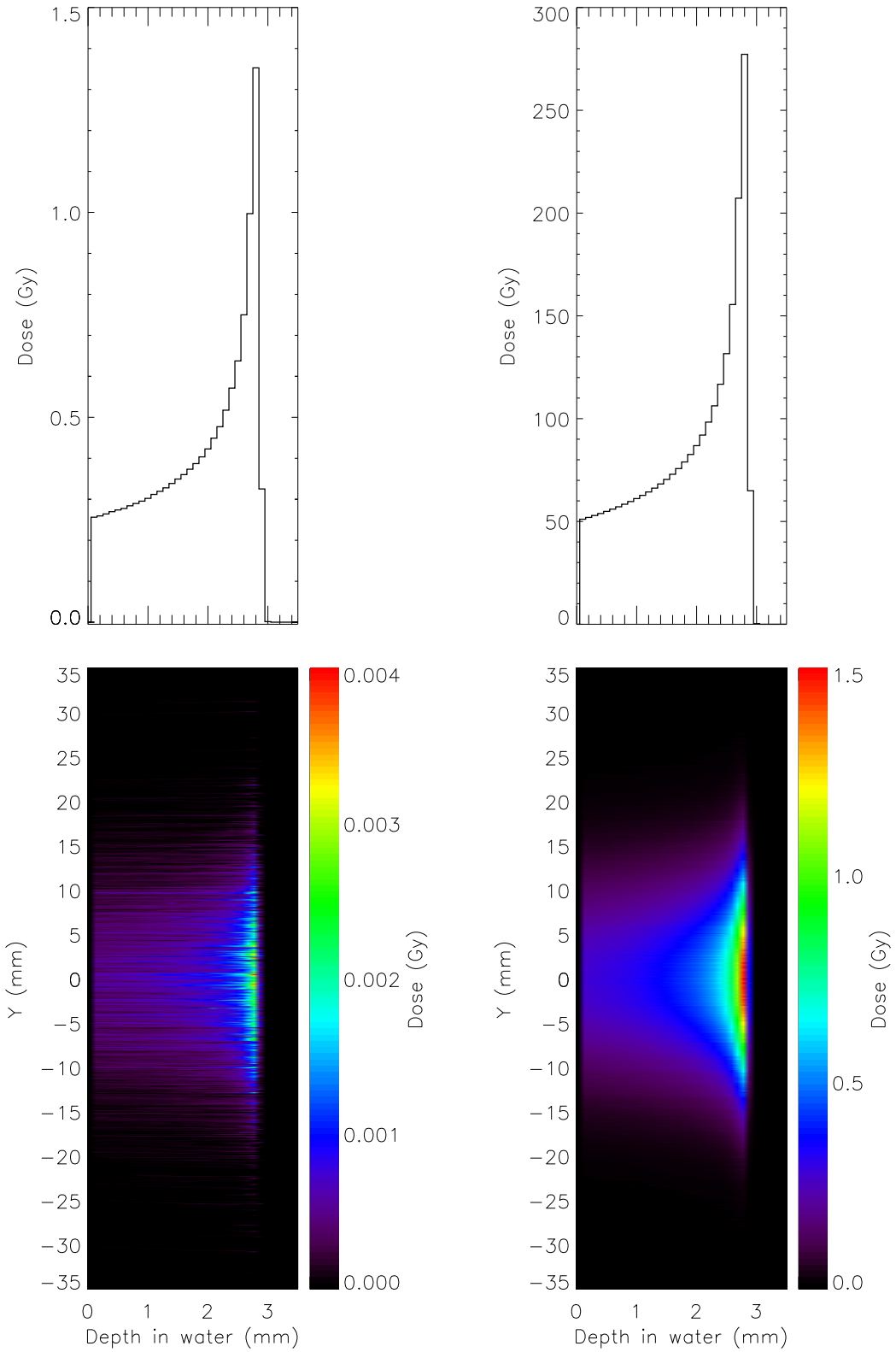

Figure 3.13: Influence of Havar® on depth-dose profile (top) and 2D distribution (bottom) of 17-MeV protons in water in the target central slice (left) and in the entire target (right).

Chapter 4

Conclusions

4.1 Work results

This work is focused on cyclotron proton beams for radiobiology. The scientific basis of a viability study for the implementation of a cyclotron-based radiobiology facility, considering an 18-MeV proton cyclotron, and particularly the one installed at ICNAS. We started from an already structured Geant4-based code and validated it against well-established Monte-Carlo based codes, as SRIM/TRIM, and theoretical expressions, as equation 1.2. Then, we continued manipulating the code to yield dose profiles and 2D distributions.

We can therefore divide this work in two main phases, the validation phase and the dose estimation phase. All work following validation was strongly influenced by the sequence of the informations about the cyclotron beam characteristics.

During the first phase, simulations were performed to validate the code for either proton range and proton beam lateral scattering. The former was validated against data from SRIM/TRIM and the latter against the theoretical σ_θ of proton angular distribution, predicted by equation 1.2. Proton range was clearly validated, as seen in Fig. 2.3. The curve correspondent to simulated data remarkably matches the curve correspondent to data obtained with TRIM. Also, either in Bragg curve and in 2D dose distribution of Fig. 2.3 it is possibly to observe a depression right before the Bragg peak, which corresponds to the decrease of protons energy below Coulomb energy for collisions with target oxygen. Passed this point, protons are scattered mainly by interactions with target nuclei. Beam lateral scattering was also validated considering the theoretical expected values.

The second phase itself can be subdivided in several parts, not necessarily subsequent to each other. Right after code validation we began to run simulations to build dose profiles obtained with pencil beam protons from ideal point sources. This would give us a reference for comparison when calculating doses delivered by beams with dispersion from non-ideal sources. Using beams and sources with these properties, we also did simulations to study the effect of target density variation on depth-dose profiles. Fig. 3.4 and Fig. 3.7 show such effect for different beam energies. One can observe that density variation influences depth-dose curves peak location and that such influence is higher for higher energies, i.e., the difference in peak location is equal to some micrometer in case of proton energies of about 18 MeV, whereas it corresponds to more than a centimeter if the beam energy is 200 MeV.

This a very important result because variations in human tissue density can also occur during a radiotherapy treatment with several sessions (fractionated radiotherapy). If such variations are not taken into account between sessions, then one can be irradiating healthy tissue without being aware and creating cold spots in the tumor. This difference is crucial because an insuffiecient irradiation in the tumor contributes to its relapse and dose in the healthy tissue induces undesirable side effects, including potential late cancer.

The simulations using beams with dispersion from non-ideal sources were an approximation to the cyclotron beam characteristics. They were based on the first estimation of beam dispersion and energy after leaving the target [Alv10a]. There were several simulations made using these considerations. The first meant to study the depth-dose profiles in four distinct radius of a cilindric water target for a beam with dispersion (Fig. 3.9). From it we can conclude that the dose is far more concentrated in small radii, being around 10 times higher in a 1-mm radius than in a 25-mm radius. The results are similar for 17- and 17.5-MeV proton beams, the peak being slightly shifted to the left for 17-MeV protons.

Another set of simulations took place for calculating dose deposition in 3D. The dose was registered voxel by voxel, these being 100-μm^3 cubes (Fig 3.13). A comparative study was made to analyze the dispersion caused by Havar®. Further corrections were not made, like simulating beam dispersion after passing through set of materials in the beam port (section 3.1) due to lack of time and computational resources. Nevertheless, such simulations allow us to have a first glance on dose values delivered by cyclotron beams to a water target.

The overall conclusion of this simulation work is that the cyclotron beam dose is too high for using in radiobiology. With a current of 150 μA, the flux is around 1×10^{15} protons per second. All doses calculated in this work are for 10^6 protons hitting the target. So, in order to estimate which dose will be delivered by 1×10^{15} proton, we must multiply the doses by 10^9. This means the result would be, in most cases, doses of GGy in only one second (for the case of an unrealizable, perfectly shaped pencil-beam).

The particular case of the calculus of 3D dose is the one with more interest because we can get the maximum dose in a 100 μm voxel of the target and it is that value we will use from this point on for our calculus. Our reference is the standard value for fractionated radiotherapy, which is 2 Gy per fraction [Ste07a]. In case Havar® is not present, the maximum dose for 10^6 protons is 0.0278234 Gy. Multiplying this by 10^9, we obtain 27.8234×10^6 Gy. This is a very high value of dose to be delivered in only one second. In case Havar® is present, the maximum dose for 10^6 protons is 0.00383697 Gy. Multiplying by 10^9, we get 3.83697×10^6 Gy. It is nearly 10 times smaller than the previous value, but it is still too high.

One way to overcome this excessive dose is to reduce cyclotron beam current. If we consider a current of 15 μA instead of 150 μA, the dose will also decrease 10 times. So, we get 2.78234 MGy without Havar® and 0.383697 MGy with it. Another solution to reduce even further these values may be to deviate the target from the beam center and make use of beam fringes, since we have already concluded that it is in the center that more dose is delivered (Fig. 3.9). Fig. 4.1 represents a way to make it possible. When leaving the cyclotron, the beam is, as already mentioned, approximately Gaussian with 80% of protons within 10 mm. Admitting that 10% of particles are beyond 5 mm on each side of the beam axis, we can make use of such particles to irradiate the target. The distance from cyclotron to the slit center was set as 2.4 m.

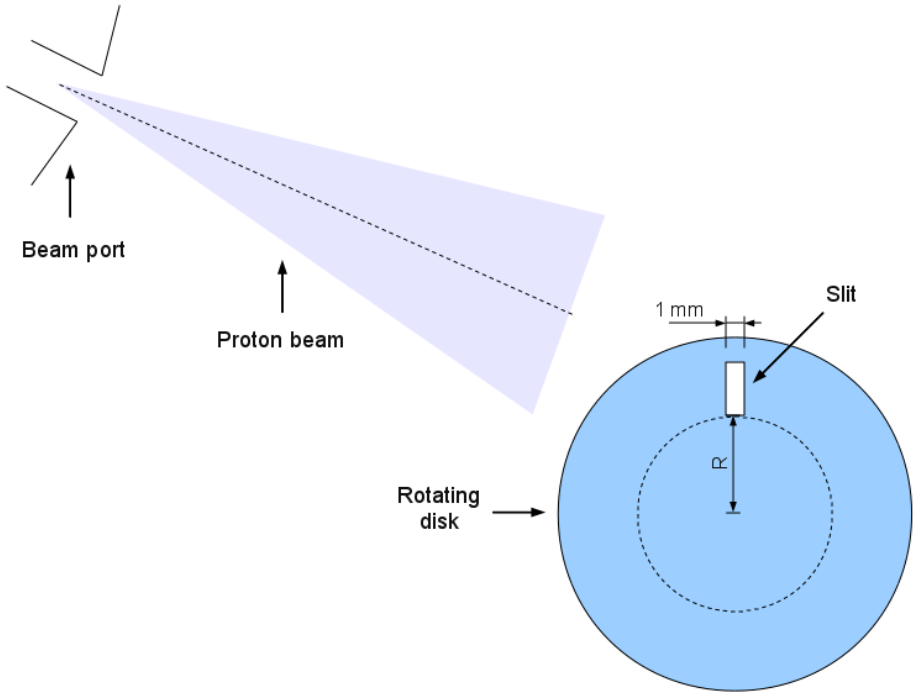

Figure 4.1: Schematic representation of a setup configuration to allow for the delivery of low doses. The target is situated under the rotating disk, which is, in turn, deviated from the beam axis. The rotating disk, with 350-mm radius, has a slit of 1-mm width and R = 300 mm. The distance from cyclotron exit and the slit center is 2.4 m.

4.2 Future work

This study had as goal to study the viability of implementing a setup at ICNAS. Further work shall be performed to confirm and re-evaluate the conclusions presented here, there are some things that can be done.

The code used is based on a hadrontherapy example from Geant4 from 2005. When running the simulations in Geant4 9.3, in the verbosity there were messages alerting for the fact that some classes are already obsolete and that they will be removed with the next major release of Geant4. So, our code must be updated and we may try to run the same simulations we did here using other physics and compare the outcomes.

One of the possibilities that may arise from the implementation of this setup is the chance to determine the accuracy of proton range using post-treatment PET [Kno10]. This can be done because positron-emitter and gamma production reactions occur when protons hit a target [Bee03]. Table 4.1 lists some of the most relevant of those reactions.

Positrons resulting from these reactions can be detected with the RPC-PET (resistive plate chamber[1]-PET) that is being developed at Laboratório de Instrumentação e Física Experimental de Partículas (LIP) [Bla06]. Its submillimetric spatial resolution and high sensitivity makes it a potential dedicated animal PET.

The results achieved with the simulation code showed that this project is now at the stage where a next-step, full-setup implementation can be fullfilled.

[1] The resistive plate chamber is a gaseous particle detector developed for high energy physics.

Table 4.1: Relevant positron-emitter production reactions; from [Bee03].

Nuclear reactions	**Threshold energy (MeV)**	**Half-life time**	**Positron Max. Energy (MeV)**
^{16}O(p,pn)^{15}O	16.79	2.037	1.72
^{16}O(p,2p2n)^{13}N[a)]	5.66[c)]	9.965	1.19
^{14}N(p,pn)^{13}N	11.44	9.965	1.19
^{12}C(p,pn)^{11}C	20.61	20.39	0.96
^{14}N(p,2p2n)^{11}C[a)]	3.22[c)]	20.39	0.96
^{16}O(p,3p3n)^{11}C[b)]	27.50[c)]	20.39	0.96

[a)] (p,2p2n) is inclusive of (p,α)
[b)] (p,3p3n) is inclusive of (p, α pn)
[c)] Listed thresholds refer to (p, α) and (p, α pn)

Appendices

Appendix A

Software and hardware used

A.1 Hardware

Machines used for performing the simulations necessary to this work are listed in Table A.1).

Table A.1: Machines used to perfom the simulations

	CPU	Number of cores	RAM memory
Machine 1	Intel® Pentium® Dual-Core T4200 2.0GHz	2	4 GB
Machine 2	Intel® 2140 1.60GHz	2	4 GB
Machine 3	Intel® Core™ 2 Quad Q6600 2.40GHz	4	4 GB

A.2 Geant4 simulation toolkit

Geant4 is a Monte-Carlo based software toolkit that simulates the passage of particles through matter [Ago03, All06]. It is a very flexible solution with innumerous models of physics processes in a wide range of energies [Ago03]. It can cover hadronic, electromagnetic and optical interactions and has libraries to a large set of materials, elements and long-lived particles [Ago03, All06]. It is designed to be used as object-oriented language and is implemented in C++ [Ago03].

The hadronic interactions with Geant4 are divided in three major groups: (1) cascade state, (2) pre-equilibrium state, and (3) equilibrium state. Each state has its own models, but for some cases it is not necessary to have a model for each state. For example, interactions at low energy ($<$ 100 MeV) can be modelized without the cascade phase [Wri10, Ago03]. The cascade state describes the intra-nuclear projectile-nucleon and nucleon-nucleon interactions after the projectile enters the nucleus. The two main models for this phase are the Bertini cascade and binary cascade. The main code for modelization of pre-equilibrium state is the precompound model that takes a nucleus from a highly-excited set of particle-hole states down to equilibrium energy by emitting protons, neutrons, deuterons, tritium nuclei, helium-3 nuclei, and alphas [Wri10]. The final phase, the equilibrium state, is known also as nuclear evaporation or nucleus de-excitation phase. After the pre-equilibrium phase, the nucleus is supposed to be left in an equilibrium state, in which the excitation energy is shared by a large number of

nucleons. If the excitation energy is higher than the separation energy[1], it can still eject nucleons and light particles (deuterons, tritium nuclei, helium-3 nuclei, and alphas) [Gea09]. The generalized evaporation model (GEM) is an example of an evaporation model.

A.3 Other software

Other software used is listed below:

- **Operating system**: openSuse 11.2 64-bit version (Linux kernel 2.6.31.12)[2]
- **Library for high energy physics**: CLHEP version 2.0.4.5.
- **C++ compiler**: GCC version 4.4.1
- **Geant4 visualization system**: HepRApp version 3.15.0
- **Data analysis**: ROOT framework version 5.26/00 and IDL version 7.0.6

[1] Separation energy is the energy needed to remove a nucleon or other particle from a nucleus

[2] Other versions of openSuse were also used, but almost all simulations were done with openSuse 11.2 64-bit version

used

Appendix B

Havar®

Havar® was originally developed in the late 1940's by the Hamilton Watch Company as an 'unbreakable' mainspring material [Rob03]. As watches moved from spring to battery power, thin Havar® strip found a second life in high strength, non-magnetic, corrosion resistant pressure sensing diaphragms for process control equipment [Rob03].

According to the technical sheet of Havar® [HPM], this material is a heat treatable cobalt base alloy that provides very high strength. The alloy has excellent corrosion resistance and is non-magnetic. Applications have included pressure diaphragms, power springs, gap spacers in magnetic heads, and target foils in nuclear physics [HPM].

Table B.1: Nominal composition of Havar®. After [HPM].

Element	**Elemental percentage**
Cobalt	42.0%
Chromium	19.5%
Nickel	12.7%
Tungsten	2.7%
Molybdenum	2.2%
Manganese	1.6%
Carbon	0.2%
Iron	Balance

Table B.2: Physical properties of Havar®. After [HPM].

Property	**Value**
Density	8.304 g cm^{-3}
Melting point	1480℃
Electrical resistivity @ R. T.	92.0 $\mu\Omega$ cm
Thermal expansion coefficient (0℃ to 50℃)	12.5 $\times$ 10^{-6} $℃^{-1}$
Thermal conductivity	13.0 W m^{-1} K
Magnetic attraction	none

Bibliography

[Ago03] S. Agostinelli *et al.* Geant4: A simulation toolkit. *Nucl Instrum Meth A*, 506(3):250–303, 2003.

[All06] J. Allison *et al.* Geant4 developments and applications. *IEEE Trans Nucl Sci*, 53(1):270–278, 2006.

[Alv10a] F. Alves, 18th June 2010. Private communication.

[Alv10b] F. Alves, 6th July 2010. Private communication, information given by Michel Guillot, Field Engineer from IBA.

[Ama10] U. Amaldi, R. Bonomi, S. Braccini, M. Crescenti, A. Degiovanni, M. Garlasché, A. Garonna, G. Magrin, C. Mellace, P. Pearce, G. Pittà, E. Rosso, S. V. Andrés, R. Wegner, M. Weiss, and R. Zennaro. Accelerators for hadrontherapy: From Lawrence cyclotrons to linacs. *Nuclear Instruments and Methods Research A*, 620:563–577, 2010. (review).

[Bee03] J. Beebe-Wang, P. Vaska, F. A. Dilmanian, S. G. Peggs, and D. J. Schlyer. Simulation of proton therapy treatment verification via pet imaging of induced positron-emitters. In *IEEE Nuclear Science Symposium/Medical Imaging Conference*, Portland, November 2003.

[Bla06] A. Blanco, N. Carolino, C. M. B. A. Correia, L. Fazendeiro, Nuno C. Ferreira, M. F. Ferreira Marques, R. Ferreira Marques, P. Fonte, C. Gil, and M. P. Macedo. RPC-PET: A new very high resolution PET technology. *IEEE T Nucl Sci*, 53(5):2489–2494, 2006.

[Boa03] Board of the Faculty of Clinical Oncology - The Royal College of Radiologists. Equipment, workload and staffing for radiotherapy in the UK 1997-2002. Online, London, September 2003. Available August 2010 at `http://www.rcr.ac.uk/publications.aspx?PageID=149&PublicationID=185#Anchor-49575`.

[Boy08] P. Boyle and B. Levin. World Cancer Report 2008. Technical report, International Agency for Research on Cancer - World Health Organization, Lyon, 2008.

[Cre05] P. Crespo. *Optimization of In-Beam Positron Emission Tomography for Monitoring Heavy Ion Tumor Therapy*. PhD thesis, Technische Universität Darmstadt, Darmstadt, Germany, 2005.

[CRU10a] Cancer Research UK. Demographic facts for the world population. Online, August 2010. Last update: August 2010. Available at `http://info.cancerresearchuk.org/cancerstats/world/demographics/index.htm#source1`.

[CRU10b] Cancer Research UK. Key facts for all cancers combined. Online, August 2010. Last update: August 2010. Available at `http://info.cancerresearchuk.org/cancerstats/keyfacts/Allcancerscombined/018212#All`.

[DK07] T. F. Delaney and H. M. Kooy, editors. *Proton and Charged Particle Radiotherapy*, pages ix–x. Lippincott Williams & Wilkins, 1st edition, 2007. Preface.

[Fal62] S. Falkmer, B. Fors, and B. Larsson. Pilot study on proton irradiation of human carcinoma. *Acta Radiol*, 58:33–51, 1962.

[Fer10] J. Ferlay, H. R. Shin, F. Bray, D. Forman, C. Mathers, and D. M. Parkin. GLOBOCAN 2008, Cancer Incidence and Mortality Worldwide: IARC CancerBase No. 10. Internet, 2010. Lyon, France: International Agency for Research on Cancer. Available from: http://globocan.iarc.fr.

[Fla07] J. Flanz. Particle accelerators. In T. F. Delaney and H. M. Kooy, editors, *Proton and Charged Particle Radiotherapy*, chapter 4, pages 27–32. Lippincott Williams & Wilkins, 1st edition, 2007.

[For02] S. Forshier. *Essentials of Radiation Biology and Protection*. Delmar, New York, 1st edition, 2002.

[Fow06] J. F. Fowler. Development of radiobiology for oncology - a personal view. *Phys. Med. Biol.*, 51:R263–R286, 2006. (review).

[Gea09] Geant4 team. *Physics Reference Manual*, December 2009. Version: Geant4 9.3.

[Ger99] L. Gerweck and S. V. Kozin. Relative biological effectiveness of proton beams in clinical therapy. *Radiotherapy and Oncology*, 50:135–142, 1999.

[Ger07] L. Gerweck and H. Paganetti. Radiobiology of charged particles. In T. F. Delaney and H. M. Kooy, editors, *Proton and Charged Particle Radiotherapy*, chapter 2, pages 8–18. Lippincott Williams & Wilkins, 1st edition, 2007.

[Goi03] M. Goitein and M. Jermann. The relative costs of proton and X-ray radiation therapy. *Clin Oncol*, 15:S37–S50, 2003.

[Gol81] L. S. Goldstein, T. L. Phillips, and G. Y. Ross. Biological effects of accelerated heavy ions. II. Fractionated irradiation of intestinal crypt cells. *Radiat Res*, 86:542–558, 1981.

[Got93] B. Gottschalk, A.M. Koehler, R.J. Schneider, J.M. Sisterson, and M.S. Wagner. Multiple Coulomb scattering of 160 MeV protons. *Nucl Instrum Meth B*, 74(4):467–490, 1993.

[Got07] B. Gottschalk. Treatment delivery systems - passive beam scattering. In T. F. Delaney and H. M. Kooy, editors, *Proton and Charged Particle Radiotherapy*, chapter 5A, pages 33–40. Lippincott Williams & Wilkins, 1st edition, 2007.

[Hal06] E. J. Hall and A. J. Giaccia. *Radiobiology for the Radiologist*. Lippincott Williams & Wilkins, 6th edition, 2006.

[Hig75] V.L. Highland. Some practical remarks on multiple scattering. *Nucl. Instrum. Meth.*, 129:497, 1975.

[Hig79] V.L. Highland. Some practical remarks on multiple scattering. *Nucl. Instrum. Meth.*, 161:171, 1979.

[HPM] HPM®: Hamilton Precision Metals. *Havar®*. Available at `http://www.hpmetals.com/pdfs/Havar.pdf`.

[IBA10] Cyclone®18/9 - Moving ahead, delivering more. Online, August 2010. Available at `http://www.iba-cyclotron-solutions.com`.

[ICR80] *Radiation Quantities and Units*. ICRU Report No. 33, Bethesda, MD, 1980.

[ICR86] *The Quality Factor in Radiation Protection*. ICRU Report No. 40, Washington, 1986.

[ICR98] *Fundamental Quantities and Units for Ionising Radiation*. ICRU Report No. 60, Bethesda, MD, 1998.

[Jäk06] O. Jäkel. Heavy ion radiotherapy. In W. Schlegel, T. Bortfeld, and A.-L. Grosu, editors, *New Technologies in Radiation Oncology*, Medical Radiology - Diagnostic Imaging and Radiation Oncology, chapter 28, pages 365–377. Springer-Verlag, Heidelberg, 2006.

[Jer10] M. Jermann. Hadron therapy patient statistics. Online, August 2010. Last update: 25th March 2010. Available at `http://ptcog.web.psi.ch/patient_statistics.html`.

[Kan99] T. Kanai, M. Endo, S. Minohara, N. Miyahara, H. Koyama-ito, H. Tomura, N. Matsufuji, Y. Futami, A. Fukumura, T. Hiraoka, Y. Furusawa, K. Ando, M. Suzuki, F. Soga, and K. Kawachi. Biophysical characteristics of HIMAC clinical irradiation system for heavy-ion radiation therapy. *Int J Radiat Oncol Biol Phys*, 44(1):201–210, 1999.

[Kno10] A.-C. Knopf, K. Parodi, H. Paganetti, T. Bortfeld, J. Daartz, M. Engelsman, N. Liebsch, and H. Shih. Accuracy of proton beam range verification using post-treatment positron emission tomography/computed tomography as function of treatment site. *Int J Radiation Oncology Biol Phys*, In Press, Corrected Proof:1–8, 2010.

[Kra00] G. Kraft. Tumor therapy with heavy charged particles. *Prog. Part. Nucl. Phys.*, 45:S473–S544, 2000.

[Lag07] J.-M. Lagniel. Hadrontherapy in Europe. In *2007 Particle Accelerator Conference*, Albuquerque, USA, June 2007.

[Lar61] B. Larsson. Pre-therapeutic physical experiments with high energy protons. *Br J Radiol Suppl*, 34:143–151, 1961.

[Law30] E. Lawrence and N. Edlefsen. On the production of high speed hydrogen ions without the use of high voltage. *Science*, 72:376, 1930.

[Mot04] C. Mothersill and C. Seymour. Radiation-induced bystander effects and adaptive responses - the Yin and Yang of low dose radiobiology? *Mutation Research*, 568:121–128, 2004. (review).

[Nah07a] A. Nahum. Interactions of charged particles with matter. In P. Mayles, A. Nahum, and J. C. Rosenwald, editors, *Handbook of Radiotherapy Physics: Theory and Practice*, chapter A3, pages 35–55. Taylor & Francis, New York, 1st edition, 2007.

[Nah07b] A. Nahum. Principles and basic concepts in radiation dosimetry. In P. Mayles, A. Nahum, and J. C. Rosenwald, editors, *Handbook of Radiotherapy Physics: Theory and Practice*, chapter A6, pages 89–121. Taylor & Francis, New York, 1st edition, 2007.

[Nak10] K. Nakamura *et al.* Review of Particle Physics. *Phys. Rev. G*, 37, 2010. Online, August 2010. Available at `http://pdg.lbl.gov`.

[Nau10] J. Naumann. Pencil-beam scanning systems in particle therapy - an overview. In *PTCOG 49, Educational School*, Chiba, Japan, May 2010.

[Nör80] W. Nörenberg. Basic concepts in the description of collisions between heavy nuclei. In R. Bock, editor, *Heavy Ion Collisions*, pages 1–43. North-Holland, 1980.

[Pag04] H. Paganetti, H. Jiang, S.-Y. Lee, and H. Kooy. Accurate Monte Carlo for nozzle design, commissioning, and quality assurance in proton therapy. *Med Phys*, 31:2107–2118, 2004.

[Pag06] H. Paganetti and T. Bortfeld. Proton therapy. In W. Schlegel, T. Bortfeld, and A.-L. Grosu, editors, *New Technologies in Radiation Oncology*, Medical Radiology - Diagnostic Imaging and Radiation Oncology, chapter 27, pages 345–363. Springer-Verlag, Heidelberg, 2006.

[Pag09] H. Paganetti. Biological uncertainties in proton (ion) therapy. In *A Symposium on the Promises and Perils of Proton Radiotherapy*, Baltimore, USA, May 2009.

[Ped00] E. Pedroni. Latest developments in proton therapy. In *Proceedings of EPAC 2000*, pages 240–244, Vienna, Austria, 2000.

[Ped07] E. Pedroni. Treatment delivery systems - pencil beam scanning. In T. F. Delaney and H. M. Kooy, editors, *Proton and Charged Particle Radiotherapy*, chapter 5B, pages 40–49. Lippincott Williams & Wilkins, 1st edition, 2007.

[pFa10] Particle therapy facilities in operation (incl. patient statistics). Online, August 2010. Last update: 31st July 2010. Available at `http://ptcog.web.psi.ch/ptcentres.html`.

[pro10] Particle therapy facilities in a planning stage or under construction. Online, August 2010. Last update: 31st July 2010. Available at `http://ptcog.web.psi.ch/newptcentres.html`.

[Raj95] M. R. Raju. Proton radiobiology, radiosurgery and radiotherapy. *Int J Radiat Biol*, 67(3):237–259, 1995. (review).

[Rob03] Mark Robinson. Havar® a New, Old Co-Cr Biocompatible Alloy for Implants. In Sanjay Shrivastava, editor, *Medical Device Materials: Proceedings of the Materials & Processes for Medical Devices Conference*, pages 324–328, Anaheim, California, USA, September 2003. ASM International.

[Sch91] T. Schwab. *Transport von Schwerionen durch Materie innerhalb ionenoptischer Systeme*. PhD thesis, University of Gießen, Gießen, 1991. GSI report 91-10.

[Sch06] W. Schlegel. New technologies in 3D conformal radiation therapy: Introduction and overview. In W. Schlegel, T. Bortfeld, and A.-L. Grosu, editors, *New Technologies in Radiation Oncology*, Medical Radiology - Diagnostic Imaging and Radiation Oncology, chapter 1, pages 1–6. Springer-Verlag, Heidelberg, 2006.

[Sch10] G. Schettino, M. Folkard, B. Vojnovic, A. Michette, and K. M. Prise. X-ray microbeams for radiobiological studies: Current status and future challenges. In *PIERS 2010 Xi'an - Progress In Electromagnetics Research Symposium Proceedings*, pages 56–60, Xi'an, China, March 2010. The Electromagnetics Academy.

[Seu05] J. P. Seuntjens, W. Strydom, and K. R. Shortt. Dosimetric principles, quantities and units. In E. B. Podgoršak, editor, *Radiation Oncology Physics: A Handbook for Teachers and Students*, chapter 2, pages 45–70. International Atomic Energy Agency, Vienna, 1st edition, 2005. Available August 2010 at `http://www-naweb.iaea.org/nahu/dmrp/syllabus.shtm`.

[She08] D. M. Shepard, C. Yu, M. Murphy, M. R. Bussière, and F. J. Bova. Treatment planning for stereotactic radiosurgery. In L. S. Chin and William F. Regine, editors, *Principles and Practice of Stereotactic Radiosurgery*, chapter 7, pages 69–90. Springer, New York, 2008.

[Smi06] A. R. Smith. Proton therapy. *Phys. Med. Biol.*, 51:R491–R504, 2006. (review).

[SRI10] SRIM - The Stopping and Range of Ions in Matter. Online, August 2010. Last update: 14th September 2006. Available at `http://www.srim.org/SRIM/SRIMINTRO.htm`.

[Ste07a] G. Steel. Dose fractionation in radiotherapy. In P. Mayles, A. Nahum, and J. C. Rosenwald, editors, *Handbook of Radiotherapy Physics: Theory and Practice*, chapter B9, pages 163–177. Taylor & Francis, New York, 1st edition, 2007.

[Ste07b] G. Steel. Radiobiology of tumours. In P. Mayles, A. Nahum, and J. C. Rosenwald, editors, *Handbook of Radiotherapy Physics: Theory and Practice*, chapter B7, pages 127–148. Taylor & Francis, New York, 1st edition, 2007.

[Sui03] H. Suit, S. Goldberg, A. Niemierko, A. Trofimov, J. Adams, H. Paganetti, G. T. Y. Chen, T. Bortfeld, S. Rosenthal, J. Loeffler, and T. Delaney. Proton beams to replace photon beams in radical dose treatments. *Acta Oncologica*, 42(8):800–808, 2003.

[Sui07] H. Suit and W. Chu. History of charged particle radiotherapy. In T. F. Delaney and H. M. Kooy, editors, *Proton and Charged Particle Radiotherapy*, chapter 1, pages 1–7. Lippincott Williams & Wilkins, 1st edition, 2007.

[Sun05] N. Suntharalingam, E. B. Podgoršak and J. H. Hendry. Basic radiobiology. In E. B. Podgoršak, editor, *Radiation Oncology Physics: A Handbook for Teachers and Students*, chapter 14, pages 485–504. International Atomic Energy Agency, Vienna, 1st edition, 2005. Available August 2010 at `http://www-naweb.iaea.org/nahu/dmrp/syllabus.shtm`.

[Tep77] J. Tepper, L. Verhey, and M. Goitein et al. In vivo determinations of RBE in a high energy modulated proton beam using normal tissue reactions and fractionated dose schedules. *Int J Radiat Oncol Biol Phys*, 2:1115–1122, 1977.

[Tob42] C. A. Tobias, D. C. Van Dyke, and M. E. Simpson. Irradiation of the pituitary of the rat with high energy deuterons. *Am J Roentgenol Radium Ther Nucl Med*, 72:1–21, 1942.

[Tob52] C. A. Tobias, H. O. Anger, and J. H. Lawrence. Radiological use of high energy deuterons and alpha particles. *Am J Roentgenol Radium Ther Nucl Med*, 67:1–27, 1952.

[Tob58] C. A. Tobias, J. H. Lawrence, J. L. Born, R. McCombs, J. E. Roberts, H. O. Anger, B. V. A. Low-Beer, and C. Huggins. Pituitary irradiation with high energy proton beams: A preliminary report. *Cancer Res*, 18:121–139, 1958.

[Tsa74] Y.-S. Tsai. Pair production and bremsstrahlung of charged leptons. *Rev Mod Phys*, 46(4):815–851, 1974.

[Tso07] E. T. M. Tsoi and J. Flanz. Facility design. In T. F. Delaney and H. M. Kooy, editors, *Proton and Charged Particle Radiotherapy*, chapter 4, pages 19–26. Lippincott Williams & Wilkins, 1st edition, 2007.

[Ver06] L. Vergara, J. Olivares, E. Iborra, M. Clement, A. Sanz-Hervás, and J. Sangrador. Effect of rapid thermal annealing on the crystal quality and the piezoelectric response of polycrystalline AlN films. *Thin Solid Films*, 515:1814–1818, 2006.

[Web96] U. Weber. *Volumenkonforme Bestrahlung mit Kohlenstoffionen zur Vorbereitung einer Strahlentherapie*. PhD thesis, University of Kassel, Kassel, 1996.

[Wid09] M. Wideł, W. Przybyszewski, and J. Rzeszowska-Wolny. Radiation-induced bystander effect: The important part of ionizing radiation response. Potential clinical implications. *Hig Med Dosw*, 63:377–388, 2009. (review).

[Wil46] R. R. Wilson. Radiological use of fast protons. *Radiology*, 47:487–491, 1946.

[Wri10] D. Wright. Hadronic Physics I. Online, August 2010. SLAC Geant4 Tutorial.

[Zie08] J. F. Ziegler, J. P. Biersack, and U. Littmark. *The Stopping and Range of Ions in Solids*. Pergamon Press, New York, 2008.

Acknowledgments

This work would not have been possible without the dedication and endeavour of all people who were involved in it, and the collaboration between institutions was determinant for accomplishing the initial goals.

My supervisor, Prof. Dr. Rui Ferreira Marques, and my co-supervisors, Prof. Dr. Francisco Alves and Prof. Dr. Paulo Crespo supported me throughout this quest, sharing their knowledge and providing all the help I needed. Also, their enthusiasm and dedication were remarkable and an actual example to me. Thank you.

I thank Prof. Luís Metello for establishing the institutional contacts that made this project a reality.

Many thanks to Prof. Dr. Gerhard Kraft, Eng. Wolfgang Becher and Dr. Michael Scholz from GSI, Darmstadt, for the informations shared and for the availability shown for collaborating with this work.

I also would like to thank Prof. Dr. Filomena Botelho for all the support and the disposal to collaborate with this project.

LIP contribution was unvaluable, welcoming us and providing the computational resources for meeting the goals of this work. For this and for all the support, many thanks. I also express my gratitude to ISEC for the availability shown for giving their support.

Finally, but no less important I would like thank to my family. Aos meus pais, em especial, por providenciarem as condições para o meu sucesso enquanto estudante do curso de Engenharia Biomédica em Coimbra. Aos meus irmãos e aos meus avós pelo apoio e pelo carinho nesta longa jornada. A todos vós, muito obrigada. A ti, Marco, por toda a paciência, encorajamento e apoio em particular neste último ano. Sem ti a meu lado, nunca teria chegado tão longe.